

# Hausmannite–Carbon Nanofiber Composite Electrocatalyst for High Areal-Discharge Energy Rechargeable Zinc–Air Battery

Augustus K. Lebechi, Lesego Gaolatlhe, Thapelo P. Mofokeng, Aderemi B. Haruna, Adewale K. Ipadeola, Patrick V. Mwonga, Oluwatosin E. Bankole, Oluwafunmilola Ola, and Kenneth I. Ozoemena\*



Cite This: *ACS Omega* 2024, 9, 39119–39133



Read Online

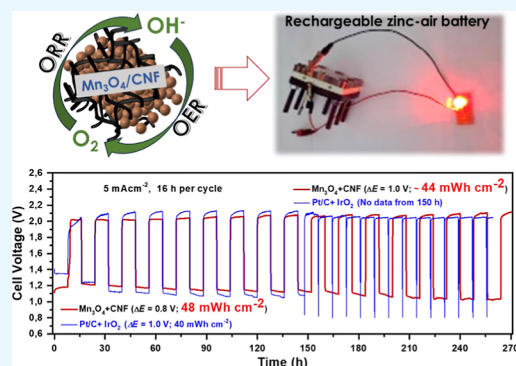
ACCESS |

Metrics & More

Article Recommendations

Supporting Information

**ABSTRACT:** Rechargeable zinc–air batteries (RZABs) have been described as one of the most viable next-generation battery technologies, especially due to their low cost, high capacity, and being environmental-friendly. In this work, hausmannite  $\text{Mn}_3\text{O}_4$  nanoparticles, obtained from low-cost commercial electrolytic manganese dioxide, were dispersed on conductive multiwalled carbon nanotubes (CNTs) and carbon nanofibers (CNFs) and investigated for oxygen reduction reaction (ORR) and oxygen evolution reaction (OER) in an alkaline medium and then applied in RZAB cell. The high performance of the CNFs (in terms of electron transfer kinetics) over the CNTs has been associated with its inherent defects and nitrogen content. Density functional theory (DFT) calculations predict that CNF give higher partial density of states (PDOS, i.e., 67 eV vs 51 eV for CNT) and can allow for a more favorable distribution of the d-electrons of the Mn and enhanced synergistic effect with  $\text{Mn}_3\text{O}_4$  for weaker adsorption energies and p-band centers of the oxygen intermediates ( $\text{O}^*$ ,  $\text{OH}^*$ , and  $\text{OOH}^*$ ). In a proof-of-concept,  $\text{Mn}_3\text{O}_4 + \text{CNF}$  was investigated as the air cathode for RZAB in a micro-3D-printed cell configuration. The RZAB showed good performance in terms of open circuit voltage (OCV = 1.77 V), areal-discharge energy ( $\geq 40 \text{ mW h/cm}^2_{\text{geometric}}$ ) and cycling stability ( $\sim 25$  cycles at 8 h per cycle for 140 h at  $10 \text{ mA cm}^{-2}$ ; and  $\sim 17$  cycles at 16 h per cycle for 270 h at  $5 \text{ mA cm}^{-2}$ ) better than 100 catalysts used in RZAB cells in recent articles including the state-of-the-art Pt/C– $\text{IrO}_2$  catalysts. The findings here provide fresh physicochemical perspectives on the future design and utility of CNFs for developing Mn-based RZABs that meet or even outperform the new literature-recommended benchmark areal-discharge energy density of  $35 \text{ mW h/cm}^2_{\text{geometric}}$  at  $10 \text{ mA cm}^{-2}$  current loading for any possible application in real devices.



## 1. INTRODUCTION

There is inherent uncertainty from the dependence of green energy on variations in weather patterns. This intermittency thereof of renewable energy sources such as wind, solar, hydropower, and waves necessitates economical and efficient devices or systems for energy storage and conversion in the quest for sustainable, cleaner, cheaper, and reliable energy. In this regard, rechargeable metal–air batteries, most especially rechargeable zinc–air batteries (RZABs) have generated intense research interest not only owing to their high theoretical and specific energy densities but also are safe (easy handling) and cost-effective due to the abundance of zinc from the Earth's crust and oxygen from the atmosphere. Therefore, RZABs have shown great potential as a promising technology in the quest to meet the energy needs of current and future energy-demanding devices.<sup>1</sup> Central to the efficient operation of RZABs and indeed all metal–air batteries is the oxygen electrochemistry involving the oxygen evolution reaction (OER) and oxygen reduction reaction (ORR). Herein, the molecules of oxygen undergo a reduction that is facilitated by electrons generated upon the oxidation of the

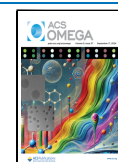
zinc anode first to form soluble zincate ions ( $\text{Zn}(\text{OH})_4^{2-}$ ) which undergoes spontaneous decomposition to insoluble zinc oxide ( $\text{ZnO}$ ) during discharge (ORR). During charging (OER) the process is reversed and molecular oxygen is freed to continue the process of discharging/charging concurrently.<sup>1,2</sup> RZABs have the fundamental advantages of being less expensive compared to lithium-ion batteries and safer (issues of lithium reactivity with air and water).<sup>3</sup> Despite these advantages, RZABs are still plagued by the fundamental challenges involving their oxygen electrochemistry in relation to finding modalities to increase the efficiency of oxygen electrocatalysis (OER and ORR).<sup>4</sup> The onus is to achieve both high performance and reversibility of the oxygen electrocatalysis process, which inherently is sluggish as a result of their

Received: June 27, 2024

Revised: July 23, 2024

Accepted: August 8, 2024

Published: September 5, 2024



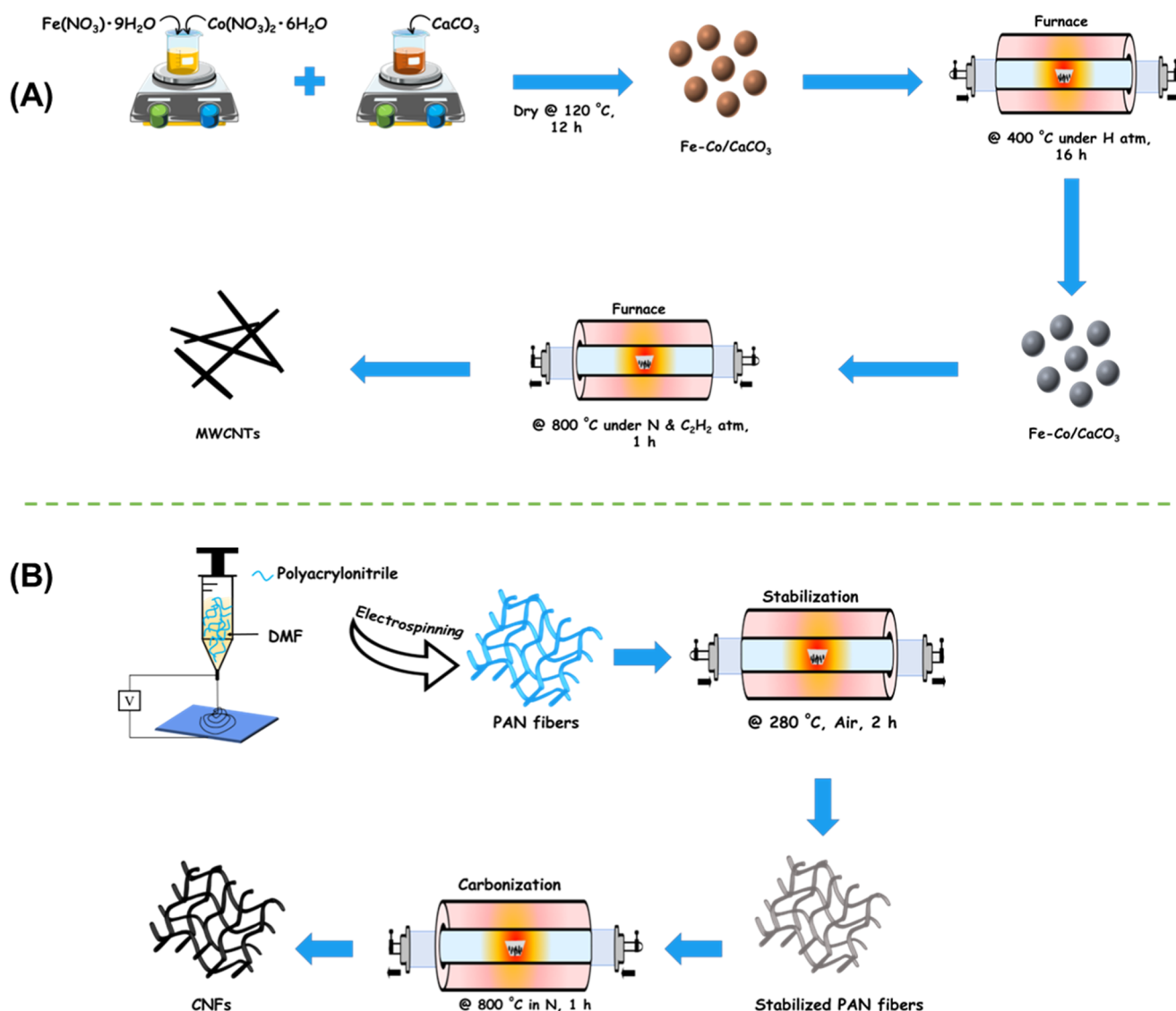


**Figure 1.** Schematic representation of the synthesis of (A) CNTs and (B) CNFs.

slow kinetics. The inherent slow kinetics can be attributed to oxygen bond cleavage with very high activation energy (498 kJ/mol), adsorption and desorption energies on a surface which affects bulk transport within the electrolyte.<sup>5</sup> Furthermore, ORR involves electron transfer processes that happen in a stepwise manner and involves oxygen containing complex intermediates such as  $O^*$ ,  $OH^*$ , and  $OOH^*$ , with varying binding energies, further complicating the kinetics of the oxygen electrochemistry.<sup>4,5</sup> The slow kinetics leads to a high overpotential, hence, the change in overpotential ( $\Delta E$ ) for reversible OER and ORR tends to be high.<sup>6</sup> From a thermodynamic viewpoint, an inverse relationship exists between  $\Delta G$  (change in free energy), overpotential and reaction rate/kinetics.<sup>7,8</sup> These conditions directly impact catalytic activity parameters such as the onset potential, half-wave potentials, and the OER benchmark potential at  $10 \text{ mA cm}^{-2}$  and obtained values in themselves provide a direct assessment of catalytic activity.

To be competitive, a catalyst must be robust, fast, and energy-efficient; it is known that the last factor (energy efficiency) is dependent on overpotential.<sup>7,8</sup> Furthermore, to enable harmonized comparisons of the performance of air-

breathing electrodes, a consistent technologically relevant areal-discharge energy standard is required.<sup>9</sup> The areal-discharge energy, which is a product of areal capacity and voltage as a performance benchmark for rechargeable zinc–air batteries, aids in the translation of lab-scale zinc–air battery results to technologically relevant battery technology. The minimum areal-discharge energy for a Zn–air cell should be approximately  $35 \text{ mW h cm}_{\text{geo}}^{-2}$  which is proportionate to a practical RZAB depth of discharge ( $\text{DOD}_{\text{zn practical}}$ ) of 20% and equivalent to Li-ion pack-level specific energy of  $120 \text{ W h kg}_{\text{pack}}^{-1}$ .<sup>10</sup> In this regard, the development of an efficient and low-cost bifunctional electrocatalyst, working in aqueous electrolytes with air providing an abundant supply of oxygen, at relatively low overpotential for enhanced areal-discharge energy density and cycling stability in RZABs is an obvious research goal.

The most employed OER and ORR electrocatalysts for air-cathodes in RZABs until recently have been noble metals and their oxides; however, both the scarcity and high costs of these catalyst materials make them nonappealing for applications in widespread commercialization.<sup>11</sup> Also, no single noble metal performs as an efficient bifunctional electrocatalyst. For

example, while platinum (Pt) shows excellent performance for ORR, in OER electrocatalysis, Pt performs poorly, and this is ascribable to the growth on the surface of the electrodes of a passivating oxide film that hinders the free flow of electrons, thereby declining the electrical conductivity of the catalyst material. In the same vein noble metal oxides of ruthenium ( $\text{RuO}_2$ ) and iridium ( $\text{IrO}_2$ ) oxides exhibit unfunctional catalytic activity for OER while showing poor activity for ORR.<sup>12</sup> Transition metal oxides, for example, manganese oxides ( $\text{MnO}_x$ ) have gained much research interest as low-cost bifunctional alternatives to noble metals and their oxides for oxygen electrocatalysis. This can be attributed to their many advantages such as abundance, low-cost, environmentally benign, and relatively good ORR activity among others.<sup>13</sup> However,  $\text{MnO}_x$  is known to suffer from low electrical conductivity which limits their utilization as electrocatalysts, in this regard, several attempts have been made to enhance the utilization of  $\text{MnO}_x$  by incorporation into conducting carbon matrices such as carbon nanofibers (CNFs),<sup>14</sup> carbon nanotubes (CNTs),<sup>15</sup> graphene oxides, and so on.<sup>16</sup>

The relevance of carbon as a conductive additive in oxygen electrocatalysis is well reported.<sup>17</sup> The low-cost carbon and low-cost  $\text{MnO}_x$  make the best marriages for developing low-cost air cathodes for RZABs. In this work, we synthesize and compare two conventional advanced carbon nanostructures, CNFs and CNTs as conducting agents for hausmannite  $\text{Mn}_3\text{O}_4$  obtained from low-cost commercial electrolytic manganese dioxide (EMD). Both  $\text{Mn}_3\text{O}_4$  + CNTs and  $\text{Mn}_3\text{O}_4$  + CNFs composites were investigated for ORR and OER, with the latter showing the best performance. Benchmarking of the ORR and OER catalytic activity parameters of the electrocatalysts was also conducted with novel results obtained.

To interrogate the high activity for  $\text{Mn}_3\text{O}_4$  + CNF over the  $\text{Mn}_3\text{O}_4$  + CNTs, we conducted theoretical experiments, density functional theory (DFT) simulations, which show that CNFs provides the platform for the distribution of the d-electrons of the Mn, and allows for weaker adsorption of the oxygen intermediates, hence lower energy is needed for desorption on the surface of the  $\text{Mn}_3\text{O}_4$  + CNF composites.<sup>18</sup> The best-performing  $\text{Mn}_3\text{O}_4$  + CNF when employed as an air-cathode for RZABs revealed satisfactory reversibility and cycling stability leading to enhanced areal-discharge energy comparable and even better than the benchmark Pt/ $\text{IrO}_2$ /C (i.e., 20 wt % Pt, 40 wt %  $\text{IrO}_2$  and 40 wt % C).

## 2. EXPERIMENTAL SECTION

**2.1. Materials and Reagents.** Commercial EMD was purchased from the Gelon Lib group, China (purity 92%). Analytical grade metal nitrates  $\text{Fe}(\text{NO}_3)_3 \cdot 9\text{H}_2\text{O}$ ,  $\text{Co}(\text{NO}_3)_2 \cdot 6\text{H}_2\text{O}$ , and Nafion perfluorinated ion-exchange resin (5 wt % mixture in aliphatic alcohol) were purchased from Sigma-Aldrich, absolute ethanol was purchased from MK chemical. A tubular quartz reactor with 51 cm  $\times$  1.9 cm i.d dimensions,  $\text{C}_2\text{H}_2$  (ethyne) gas, nitrogen, and quartz boat (120  $\times$  15 mm) were purchased from Afrox. Polyacrylonitrile (99.9%, PAN,  $M_w$  = 150,000 g/mol) was purchased from Sigma-Aldrich. Other materials used were *N,N*-dimethylformamide (DMF), potassium hydroxide (KOH) pellets, zinc acetate, ultrapure water from a Milli-Q water system, and aluminum oxide ( $\text{Al}_2\text{O}_3$ ) powder. All reagents were used without further purification.

**2.2. Synthesis of Bifunctional Electrocatalysts Composition.** **2.2.1. Synthesis of  $\text{Mn}_3\text{O}_4$ .** Commercial EMD (with

$\text{MnO}_2$  purity of 92%) was purchased from Gelon Group, China, and the tetragonal hausmannite  $\text{Mn}_3\text{O}_4$  nanoparticles were synthesized from EMD by a high-temperature annealing process (Figure S1). Herein, powdered EMD was placed in a horizontal tube furnace and ramped from room temperature to 1000 °C at a heating rate of 5 °C  $\text{min}^{-1}$  in air, and the temperature of the furnace was kept constant for 40 h.

**2.2.2. Synthesis of Multiwalled Carbon Nanotube.** Multiwalled carbon nanotube (MWCNT) synthesis was preceded by the preparation of Fe–Co/ $\text{CaCO}_3$  catalyst (Figure 1A):<sup>19</sup> Fe–Co/ $\text{CaCO}_3$  catalyst synthesis was achieved through an impregnation route using an aqueous mixture of  $\text{Fe}(\text{NO}_3)_3 \cdot 9\text{H}_2\text{O}$  (0.3 M) and  $\text{Co}(\text{NO}_3)_2 \cdot 6\text{H}_2\text{O}$  (0.3 M). The prepared precursor solution was added dropwise to a stirring solution of  $\text{CaCO}_3$  and the mixture was allowed to stir for 30 min. The resultant metal support mixture was filtered and left to dry in an oven at 120 °C for 12 h, upon cooling to room temperature the mixture was ground and sieved with a 150  $\mu\text{m}$  mesh.

The Fe–Co/ $\text{CaCO}_3$  catalyst was thereafter calcined for 16 h at 400 °C in air to decompose the nitrates in the catalyst. The Fe–Co catalysts supported on  $\text{CaCO}_3$  (Fe–Co/ $\text{CaCO}_3$ ) provides a triple-point (Fe–Co/ $\text{CaCO}_3$ / $\text{C}_2\text{H}_2$ ) reaction junction around the catalyst support interphase for enhanced decomposition and growth of the CNTs from the acetylene ( $\text{C}_2\text{H}_2$ ) gas carbon source precursor. The catalyst also helps to reduce agglomeration of the synthesized CNTs.<sup>20</sup> Synthesis of the MWCNTs followed a procedure previously reported.<sup>21</sup> During the synthesis of the MWCNTs a tubular quartz reactor was placed in a horizontal furnace, and ethylene gas ( $\text{C}_2\text{H}_2$ ) served as the carbon source precursor. In this procedure, the formation of amorphous carbon was achieved from graphitic carbon and nitrogen (carrier gas) to dilute  $\text{C}_2\text{H}_2$  to reduce the contact time between the carbon source and the catalyst. In this synthesis, 0.3 g of the catalyst was spread uniformly onto a quartz boat and subsequently placed in the center of the quartz tube. The furnace temperature was then ramped up to 800 °C at the rate of 10 °C  $\text{min}^{-1}$  under flowing  $\text{N}_2$  gas (40 mL  $\text{min}^{-1}$ ) after which  $\text{C}_2\text{H}_2$  (100 mL  $\text{min}^{-1}$ ) and  $\text{N}_2$  (240 mL  $\text{min}^{-1}$ ) were simultaneously bubbled through for 1 h. The gas bubbling was stopped, and the system was left to cool to room temperature under  $\text{N}_2$  (40 mL  $\text{min}^{-1}$ ), the quartz boat was then removed from the reactor, and the carbon deposits that formed along with the catalyst were weighed. Purification of the resulting materials to remove CaO, and residual Fe–Co particles, was undertaken using 55%  $\text{HNO}_3$  under reflux in an oil bath held at 110 °C for 4 h. After the acid treatment, the carbon materials were then filtered and washed several times with distilled water to remove residual  $\text{HNO}_3$  until a neutral pH was observed on the filtrate. The carbon materials were then dried at 120 °C for 12 h.

**2.2.3. Synthesis of CNFs.** Prior to electrospinning, a polymer blend was prepared by dissolving 10 wt % of PAN in 5.0 mL of DMF. This solution was then stirred for 24 h to obtain a homogeneous solution. The homogenized solution was placed in a syringe fitted with a hypodermic needle (inner diameter of 0.1 mm) at 0.1 mL  $\text{h}^{-1}$  flow rate and electrospun using an electrospinning setup with the high voltage power supply set at 9 kV and the tip to collector distance (T.C.D) of 15 cm. Aluminum foil was used as the collector, and the solidified fibers were collected at ambient temperature. The electrospun nanofibers were then stabilized in the air at 280 °C for 1 h and were subsequently carbonized at 800 °C for 1 h under  $\text{N}_2$  gas flow, as illustrated in Figure 1B.

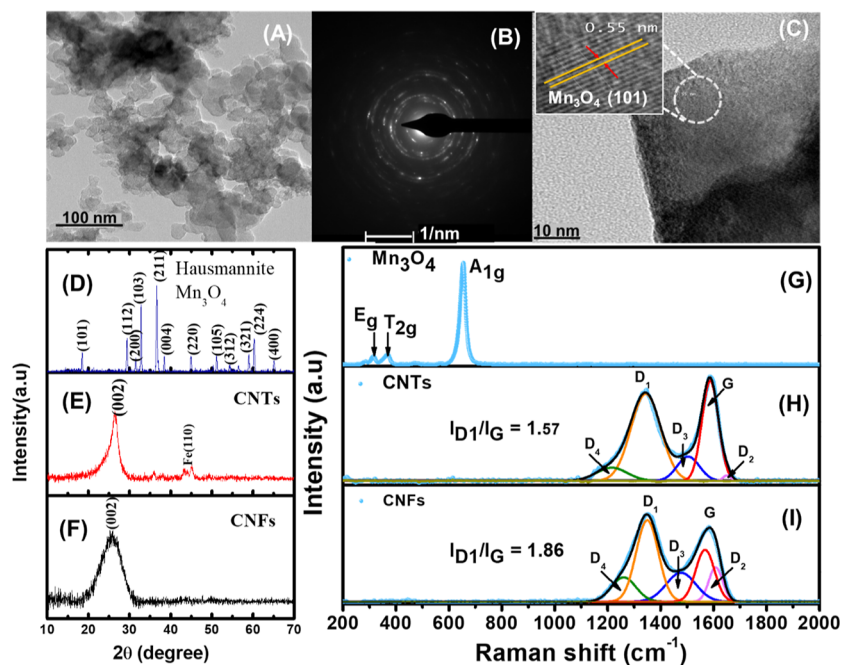


**Figure 2.** (A) Low magnification TEM image; (B) SAED pattern and (C) HRTEM image of  $\text{Mn}_3\text{O}_4$ ; XRD patterns of (D)  $\text{Mn}_3\text{O}_4$ , (E) CNTs and (F) CNFs; Raman spectra of (G)  $\text{Mn}_3\text{O}_4$ , (H) MWCNTs and (I) CNFs.

**2.3. Material Characterization.** The morphology and structural features of the synthesized nanomaterials were ascertained using X-ray diffraction (XRD) (PANalytical X'Pert powder diffractometer with  $\text{Co K}\alpha$  radiation), scanning electron microscopy (SEM) was undertaken using a Zeiss Auriga field emission scanning electron microscope, and SmartSEM software was used to obtain the images. For the EDX data, an Oxford X-max detector operating with Aztec software was employed. The transmission electron microscopy (TEM) data was obtained using a JEOL JEM 2100 at 200 kV was used. The Raman spectra were accumulated on a Bruker Raman Senterra spectrometer using a 532-nm excitation laser and a laser power of 0.2 mW. Electrochemical experiments were carried out at room temperature employing the conventional three-electrode configuration using a Bio-Logic SP300 electrochemical workstation running on EC-Lab software. A modified rotating disk electrode (RDE, GCE, diameter = 5 mm, Autolab) was employed as the working electrode. A platinum rod (Pt) and Ag/AgCl saturated (3 M KCl) were used as the counter and reference electrodes, respectively. The electrochemical impedance spectroscopy (EIS) measurements were recorded at frequencies between 100 kHz and 10 mHz with the amplitude (rms value) of the AC signal set at 10 mV. Prior to each experimental measurement, the RDE glassy carbon surface was polished to a mirror finish using alumina slurry (nanopowder, Aldrich). The catalysts ink was prepared by mixing in 1.0 mL ethanol solution containing 20  $\mu\text{L}$  of 5% nafion solution (DuPont)  $\text{Mn}_3\text{O}_4$  and nanocarbon conducting materials (CNF and MWCNT) in a 1:1 ratio to create the composites  $\text{Mn}_3\text{O}_4$  + CNF and  $\text{Mn}_3\text{O}_4$  + CNT. The mixtures were each left to stir overnight to make homogeneous ink solutions. Modification of the RDE was achieved by dropping 20  $\mu\text{L}$  of the catalyst ink on its surface to achieve a catalyst loading of 0.2  $\text{mg cm}^{-2}$  and allowing it to dry in the air for about 30 min. For all electrochemical experiments, 1.0 M KOH solution saturated

with high-purity nitrogen and oxygen was employed as the electrolyte for the OER and ORR measurements, respectively.

The fabrication of the rechargeable zinc–air battery followed a previously established procedure,<sup>22</sup> with slight modification. A micro-3D-printed cell consisted of a zinc foil (1.0 mm) anode, a mixture of 6.0 M KOH and 0.2 M zinc acetate as the electrolyte, and bifunctional electrocatalysts (i.e.,  $\text{Mn}_3\text{O}_4$  + CNF) as air cathode. The cathode was made by mixing  $\text{Mn}_3\text{O}_4$  and CNFs in a ratio of 1:1. A thick slurry of the mixture was made by adding isopropanol (180.0  $\mu\text{L}$ ), water (20  $\mu\text{L}$ ) and PTFE (20.0  $\mu\text{L}$ ), which was coated on double-placed carbon papers. The Zn plate and the carbon-paper-coated nanocatalysts are then laminated and fabricated in the micro-3D printed cell and liquid electrolyte is poured between them to make direct contact on both electrodes, before any RZAB tests.

### 3. RESULTS AND DISCUSSION

**3.1. Material Characterization.** The surface morphology and elemental composition of all of the synthesized materials were investigated using SEM and EDX, respectively. As shown in the supporting document, Figures S2 compares the SEM images of the  $\text{Mn}_3\text{O}_4$  and its EDS, CNFs, and CNTs. The materials gave the expected morphologies. Figure S2A shows the porous aggregated irregularly shaped morphology of  $\text{Mn}_3\text{O}_4$ . The EDS spectrum for  $\text{Mn}_3\text{O}_4$  (Figure S2B) reveals the elemental compositions (Mn and O) without traces of impurities. The EDS spectra for the carbon additives (CNF and CNT) are shown in Figure S3A,B. The SEM image for the CNF (Figure S2C) revealed the smooth, long cylindrical, one-dimensional structure of electrospun nanofibers. These morphological properties are attributed to the carbonization process which introduces surface defects by removing the non-carbonized components such as  $\text{H}_2\text{O}$ ,  $\text{NH}_3$ ,  $\text{CO}$ ,  $\text{CO}_2$ , and increased levels of graphitized carbon with respect to amorphous carbon.<sup>23</sup> The short branched tubes with increased surface area and defects endow faster electron transfer and enhanced conductivity. The SEM image of synthesized

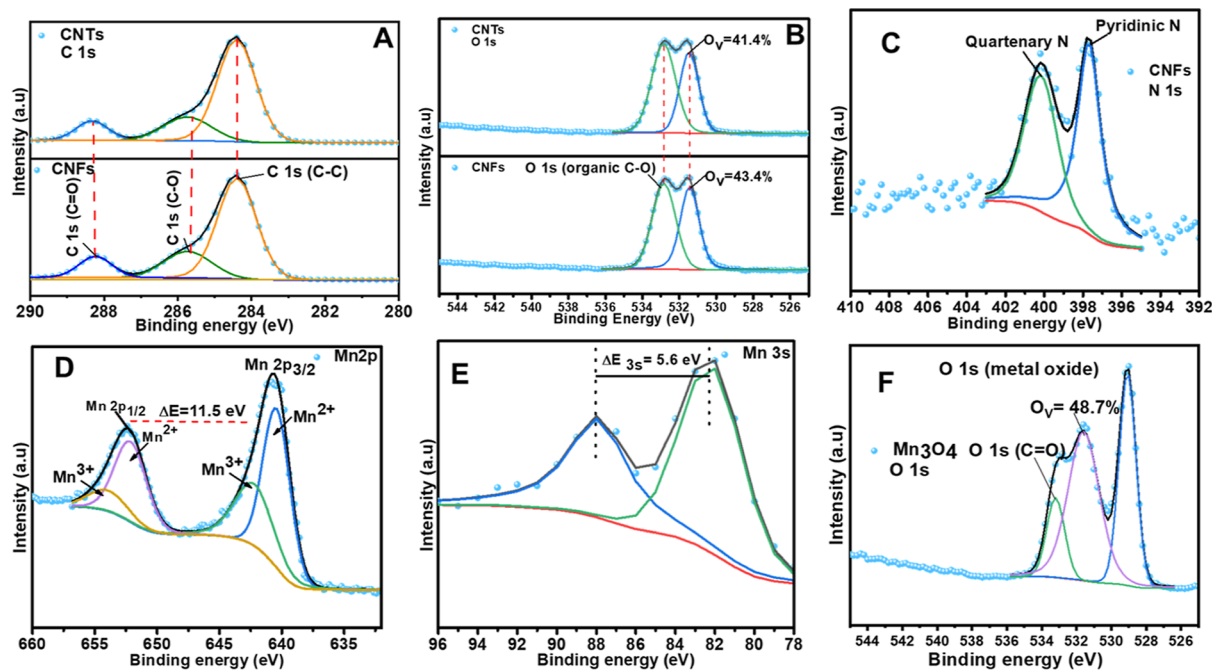


**Figure 3.** Deconvoluted XPS data for (A) C 1s spectra for CNT and CNF; (B) O 1s spectra for CNT and CNF; (C) N 1s spectra for CNF; (D) Mn 2p; (E) Mn 3s spectra; and (F) Mn 1s spectra.

MWCNTs (Figure S2D) clearly revealed the curled and entangled morphology of MWCNTs.

Further in-depth analysis of the microstructure and crystallinity of the as-synthesized  $\text{Mn}_3\text{O}_4$  catalysts was undertaken by TEM, HRTEM, and selected area (electron) diffraction (SAED) patterns as shown in (Figure 2). The typical low-magnification TEM image of pristine  $\text{Mn}_3\text{O}_4$  (Figure 2A) revealed sphere-shaped particles with sizes in the nanometer range. Further confirmation of the crystalline nature of the nanoparticles was studied using the SAED pattern (Figure 2B).

The visibly clear diffraction rings can be indexed to hausmannite  $\text{Mn}_3\text{O}_4$  and confirm the crystallinity of the as-synthesized nanomaterial. The HRTEM image (Figure 2C) reveals crystalline lattice fringes with interplanar spacing between adjacent atomic lattices of about 0.55 nm (inset: Figure 2C), attributable to tetragonal  $\text{Mn}_3\text{O}_4$  and corresponds to the  $\{101\}$  crystal plane, which is also present in the XRD data.

The typical powder XRD patterns (Figure 2D) are consistent with the  $\text{Mn}_3\text{O}_4$  nanoparticles (JCPDS card no. 00-001-1127) with a tetragonal crystal structure (space group  $141/amd$ ).<sup>24</sup> The heating procedure involved in the  $\text{Mn}_3\text{O}_4$  preparation reduces Mn to lower valence states, a phenomenon that introduces structural changes. Hence, the XRD pattern of  $\text{Mn}_3\text{O}_4$  represents a phase change from the EMD to  $\text{Mn}_3\text{O}_4$  because of the thermal treatment. Moreover, the narrow and very sharp XRD patterns of  $\text{Mn}_3\text{O}_4$  are ascribable to its high crystallinity and larger crystallite sizes, as revealed in the SAED patterns. The XRD pattern of the MWCNTs (Figure 2E) shows the characteristic pattern of graphitized carbon with Miller index (002) at a diffraction angle ( $25.94^\circ$ ) and corresponding interplanar spacing ( $\sim 0.343$  nm) (JCPDS card no. 75-1621), which is characteristic of MWCNTs.<sup>21</sup> The Fe(110) shows the presence of Fe impurities from the Fe-Co/ $\text{CaCO}_3$  catalyst inside the tube shielded from the acid during

the purification process.<sup>25</sup> The EDS (Figure S3B) also confirms the presence of Fe impurities. Interestingly, as will be seen later, the presence of Fe in the CNT did not improve the electrocatalytic performance of the  $\text{Mn}_3\text{O}_4/\text{CNT}$ . Figure 2F shows the XRD pattern of the as-synthesized CNFs with the main diffraction peak at  $2\theta = 25.7^\circ$  corresponding to the C(002) crystal plane of graphitic carbon (JCPDS card no. 65-6212). The XRD patterns of the MWCNTs exhibit a sharper and less broad peaks characteristic of the (002) plane of graphitic carbon materials, which is an indication that the MWCNTs are more crystalline than the CNFs.<sup>26</sup>

Raman spectrum of the synthesized  $\text{Mn}_3\text{O}_4$  (Figure 2G) shows three distinct peaks at approximately 658, 371, and 315  $\text{cm}^{-1}$  ascribable to the stretching  $A_{1g}$  mode of manganese oxide in  $\text{Mn}^{2+}$  ions at a tetrahedral site and the doubly degenerate  $T_{2g}$  symmetry modes, respectively. These peaks are consistent with  $\text{Mn}_3\text{O}_4$  reported in previous studies.<sup>27–29</sup> Figure 2H,I show the Raman spectra of MWCNTs and CNFs with two distinct broad peaks at approximately 1350 and 1590  $\text{cm}^{-1}$ , which correspond to the D- and G-bands, respectively. The D- and G-band of carbon materials are attributed to disordered graphene (D) and the ordered  $\text{sp}^2$ -bonded carbon (G).<sup>27,30</sup> The intensity ratio ( $I_D/I_G$ ) measured using the area under the D- and G-bands is an important parameter that gives a sensitive measure of the disorder as well as the graphitization degree of carbon materials. The  $I_D/I_G$  value of MWCNTs (1.57) is observed to be lower than that of CNFs (1.86), and the higher value obtained for CNF is due to increased defects due to the carbonization process during synthesis and the presence of electronegative nitrogen from PAN.

Nitrogen ( $\text{N}_2$ ) physisorption experiments were conducted to determine the Brunauer–Emmett–Teller (BET) surface area, pore volume, and pore size. These parameters are vital properties of electrode materials in energy storage. Figure S4A,B shows the  $\text{N}_2$  adsorption/desorption isotherms while the pore size distribution curve is shown in Figure S4C.

**Table 1. Showing Activity Parameters for the Composite Catalysts.**

Mn-based Catalysts	ECSA (cm <sup>2</sup> )	RF	$J_{s,\eta=0.35V}$ (mA cm <sup>-2</sup> )	$J_{s,\eta=0.35V}$ (mA cm <sup>-2</sup> )
Mn <sub>3</sub> O <sub>4</sub> + CNT	429.2 ± 0.4	2179 ± 0.20	4.35 ± 0.01	0.002 ± 0.01
Mn <sub>3</sub> O <sub>4</sub> + CNF	188.8 ± 0.2	958 ± 0.03	3.83 ± 0.01	0.004 ± 0.01

Typical type IV isotherms with H3-type hysteresis loop, herein ( $P/P_0 > 0.4$ ),<sup>31,32</sup> were observed which is an indication of the presence of a mesoporous structure in the CNFs and CNTs. The BET surface areas presented in Table S1 for the CNFs and CNTs were calculated to be 174.2 and 43.5, respectively. The higher BET surface area of the CNFs is ascribed to the increased defects on the surface of CNFs which is supported by the high  $I_D/I_G$  ratio from the Raman spectroscopy Figure 2H,I. The pore size distribution curves of CNFs and CNTs revealed both mesopores and macropores, as determined by the Barrett–Joyner–Halenda (BJH) method (Figure S4C). The ceaseless pore size distribution ranges between 4 and 150 nm, an indication of a direct decrease with increasing pore diameter. The pore diameter of the CNFs as determined by the BJH method ranges between 2.4 and 4.3 nm (see inset: Figure S4C), and for the CNTs the pore diameter ranges between 2.9 and 4.3 nm; these data are consistent with the mesoporous character of the as-synthesized carbon conducting materials. The discharge/charge processes of RZABs is enhanced by the mesopores by facilitating fast electrolyte ion adsorption and short diffusion distance for improved mass transfer kinetics.<sup>33</sup>

X-ray photoelectron spectroscopy (XPS) was used to characterize the surface elemental composition of the catalyst material (Mn<sub>3</sub>O<sub>4</sub>) and the conductive carbon agents (CNF and MWCNT). The XPS survey scan analysis was obtained in the binding energy range of 0 and 1300 eV, the wide survey scans (Figure S5A) revealed the surface elements on the CNF and is dominated by three peaks located at 287.40, 399.07, and 534.37 eV ascribable to C 1s, N 1s, and O 1s, respectively. For the CNTs (Figure S5B), only two peaks located at 287.91 and 533.83 eV assigned to C 1s and O 1s respectively and no N 1s peaks were observed. The wide survey scans for Mn<sub>3</sub>O<sub>4</sub> (Figure S5C) reveal the presence of Mn 3s, O 1s, Mn 3p and Mn 2p was obtained in the binding energy levels 82.29, 531.32, 52.26, and 643.94 eV respectively and is consistent with reported results.<sup>34,35</sup> As a result of multiple splitting, broad peaks were observed for Mn 3s and Mn 2p respectively and generally in the 3s region transition metal compounds show multiple peaks splitting. The broad O 1s peak is symmetrical toward its lower and higher binding energy sides. At the binding energy 53.4 eV, the Mn 3p peak characteristics of Mn<sub>3</sub>O<sub>4</sub> were observed and no evidence of peaks corresponding for other elements was observed. The C 1s spectra for CNT and CNF (Figure 3A) were dominated by three peaks located at 284.42 eV for C–C/C=C, indicating the presence of graphitic carbon,<sup>36</sup> the peak C–O at 285.88 eV and C=O/O–C=O peak at 288.44 eV corresponding to oxygen-containing functionalities such as carbonyl and carboxyl groups,<sup>37</sup> due to partial air oxidation of the CNTs and CNFs when the samples are taken out of the reactor. Deconvolution of the O 1s peaks for CNF and CNT (Figure 3B) yielded two peaks located at 531.57 eV, ascribable to oxygen vacancies due to surface defects introduced during the carbonization and calcination processes. The value obtained for the oxygen vacancy of CNFs is 43.4% which is slightly higher than that from CNT at 41.4%, the enhanced surface

defects and higher oxygen vacancy bodes well for electrocatalysis. The N 1s spectrum (Figure 3C) for the CNF was deconvoluted into two main peaks located at 397.82 eV for pyridinic nitrogen and 400.21 eV assigned to a more positively charged nitrogen with quaternary N coordination.<sup>36</sup> The Mn 2p XPS spectra (Figure 3D) showed two broad peaks at binding energies of 641.08 eV for Mn 2p<sub>3/2</sub> and 652.57 eV for Mn 2p<sub>1/2</sub>, respectively. The calculated spin orbit splitting between Mn 2p<sub>3/2</sub> and Mn 2p<sub>1/2</sub> is 11.5 eV which corresponds to reported values for hausmannite Mn<sub>3</sub>O<sub>4</sub>.<sup>38</sup> To determine the oxidation state of Mn, the Mn 2p<sub>3/2</sub> peak was further deconvoluted into two components with binding energies located at 640.46 and 642.60 eV attributed to Mn<sup>2+</sup> and Mn<sup>3+</sup>, respectively.

From the XPS spectra, the decrease in the content of Mn<sup>3+</sup> is attributed to the generation of oxygen vacancies, which causes an incomplete octahedral crystal field for trivalent manganese. Furthermore, the presence of a Mn<sup>2+</sup>/Mn<sup>3+</sup> redox couple bodes well for ORR and OER electrocatalysis as it increases the active surface area. The Mn 3s multiple splitting is prevalent among transition metals with magnitude attributed to the number of unpaired d-orbital electrons. The binding energy of the 3s level was observed at 82.60 eV with a multiple splitting value of 5.6 eV (Figure 3E) corresponding to reported values for hausmannite Mn<sub>3</sub>O<sub>4</sub>. The high-resolution O 1s spectrum is shown in (Figure 3F) and deconvoluted into three peaks. The first peak at 529.15 eV belongs to the lattice oxygen of the metal oxide bond (Mn–O–Mn), the second peak at 531.45 eV is the oxygen vacancy (O<sub>v</sub>) peak due to surface defects, the obtained value for the oxygen vacancy is 48.7%, and the peak at 532.97 eV belongs to oxygen adsorbed on carbon or OH species. The increased oxygen vacancy bodes well for electrocatalysis.

**3.2. Determining the Electrocatalytic Active Surface Area.** First, the electrocatalytic active surface area (ECSA) of each of the two electrocatalysts was measured using cyclic voltammograms (CV) at varying scan rates in order to obtain the non-Faradaic capacitive current associated with double-layer charging.<sup>39</sup> As shown in Figure S6, CVs were recorded at different scan rates. The measured charging current ( $i_c$ ) is equal to the product of the scan rate ( $\nu$ ) and the electrochemical double-layer capacitance ( $C_{DL}$ ), according to eq 1.<sup>39,40</sup>

$$I_c = \nu C_{DL} \quad (1)$$

In this regard, a plot of  $i_c$  with respect to  $\nu$  yields a straight line with a slope equal to that of  $C_{DL}$  for the composite electrocatalysts. The values obtained for the electrochemical double-layer capacitance  $C_{DL}$  for the composite electrocatalysts are 17.17 (Mn<sub>3</sub>O<sub>4</sub> + CNT) and 7.56 mF (Mn<sub>3</sub>O<sub>4</sub> + CNF). The ECSA is calculated from  $C_{DL}$  using eq 2

$$ECSA = \frac{C_{DL}}{C_s} \quad (2)$$

where  $C_s$  represents the specific capacitance of the sample, and values typically used for  $C_s$  in 1 M NaOH and KOH range between 0.022 and 0.130 mF cm<sup>-2</sup>.<sup>41,42</sup> To enable

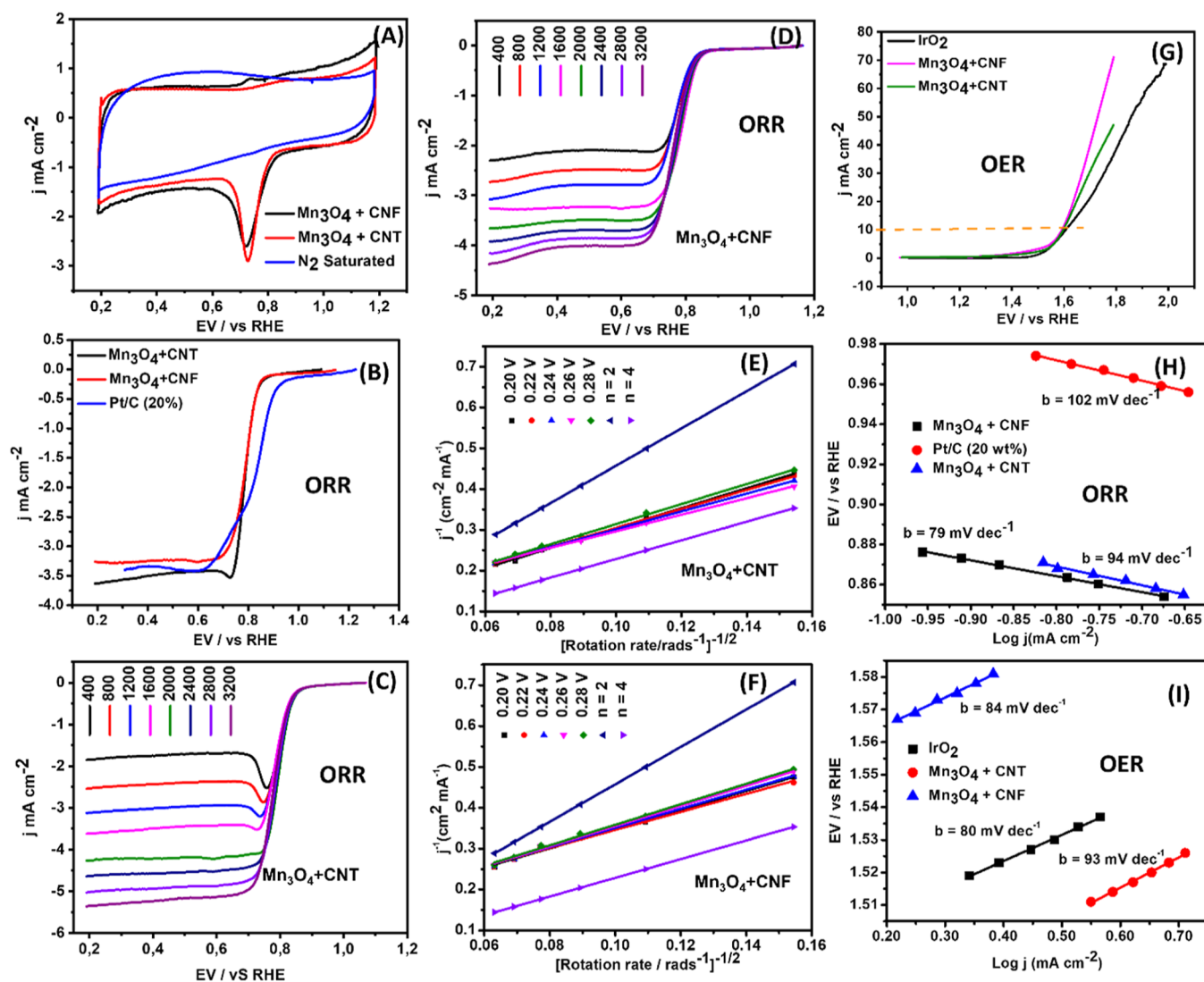


**Figure 4.** (A) Typical cyclic voltammograms of  $\text{Mn}_3\text{O}_4 + \text{CNF}$  and  $\text{Mn}_3\text{O}_4 + \text{CNT}$  catalysts measured in 1.0 M KOH electrolyte solution saturated with oxygen at 50 mV/s; (B) hydrodynamic ORR voltammograms at 1600 rpm for  $\text{Mn}_3\text{O}_4 + \text{CNT}$ ,  $\text{Mn}_3\text{O}_4 + \text{CNF}$  and Pt/C at 10 mVs<sup>-1</sup>; (C,D) hydrodynamic ORR at different speeds (400–3200 rpm) for  $\text{Mn}_3\text{O}_4 + \text{CNT}$  and  $\text{Mn}_3\text{O}_4 + \text{CNF}$ ; their corresponding Koutecky–Levich plots (E,F), respectively; (G) hydrodynamic OER voltammograms at 1600 rpm for  $\text{Mn}_3\text{O}_4 + \text{CNF}$ ,  $\text{Mn}_3\text{O}_4 + \text{CNT}$  and  $\text{IrO}_2$ ; Tafel plots of the various catalysts obtained for (H) ORR and (I) OER.

determination of the estimated surface area of the catalysts, the value of the general specific capacitance of  $C_s = 0.040 \text{ mF cm}^{-2}$  in 1 M KOH, according to typically reported values.<sup>43</sup> From the estimated ECSA values, the catalyst surface roughness factor (RF) was estimated by the ratio of the ECSA and the geometric area of the electrode,  $0.197 \text{ cm}^2$ , in this instance. The estimated ECSA and RF values for the catalysts are shown in Table 1. The specific current density per catalyst surface area ( $j_s$ ), a metric for assessing catalytic activity was also determined for the composite catalysts.<sup>44,45</sup> This is estimated from the ratio of current density per geometric area at a delineated overpotential by the RF calculated by dividing the current density per geometric area at a given overpotential by the RF according to eq 3

$$j_s = \frac{j_g}{\text{RF}} \quad (3)$$

The results obtained for the average current density per geometric area at  $\eta = 0.1 \text{ V}$  are reported in (Table 1), with standard deviations.

ECSA, RF, current density per geometric area at a given overpotential ( $J_g$ ) and specific current density per catalyst surface area ( $J_s$ ).

The catalysts in this study gave comparative results with respect to other transition metal electrocatalysts in similar studies. The rationale behind the choice of  $\eta = 0.1$  is according to previously reported device models which reported that a solar water splitting device at  $10 \text{ mA cm}^{-2}$  ideally should operate at 10% efficiency with maximum overpotential at  $\sim 0.45 \text{ V}$  for OER and HER combined.<sup>46</sup> The model assumes that  $\eta = 0.35 \text{ V}$  is for OER, leaving  $\eta = 0.1 \text{ V}$  for ORR and HER.<sup>46,47</sup> As will be seen later, the high activities of the CNT support shown in Table 1 are good for mass transport but do not translate to electrocatalytic kinetics.

**3.3. ORR and OER Activities.** The conventional three-electrode cell configuration was employed for all the

**Table 2.** Table of ORR and OER Parameters for Mn<sub>3</sub>O<sub>4</sub> + CNT and Mn<sub>3</sub>O<sub>4</sub> + CNF Electrocatalysts in a 1.0 M KOH Electrolyte Solution

Mn-based catalyst	no. of electrons	$E_{1/2}/V$ (ORR)	$b$ (mV dec <sup>-1</sup> ) (ORR)	$b$ (mV dec <sup>-1</sup> ) (OER)	$R_{ct}/\Omega$ (OER)	$E_{j=10}/V$ (OER)	$\Delta E$
Mn <sub>3</sub> O <sub>4</sub> + CNF	3.87	0.79	79	85	149.0	1.58	0.79
Mn <sub>3</sub> O <sub>4</sub> + CNT	3.98	0.79	94	93	184.6	1.59	0.80
Pt/C		0.86	102			1.61	0.75
IrO <sub>2</sub> /C				80		1.59	

electrochemical experiments involving three-electrodes which were undertaken under ambient conditions using a Bio-Logic SP300 electrochemical workstation running on electrochemical laboratory (EC-Lab) software. CVs (Figure 4A) for the RDE (GCE) modified with the electrocatalysts were measured in 1.0 M KOH electrolyte solution that was first saturated with O<sub>2</sub> using 50 mV s<sup>-1</sup> as the scan rate. Both Mn<sub>3</sub>O<sub>4</sub> + CNT and Mn<sub>3</sub>O<sub>4</sub> + CNF showed similar responses toward ORR at a reduction peak potential of ~0.75 V versus RHE. Figure 4B compares the hydrodynamic ORR at 1600 rpm for the Mn<sub>3</sub>O<sub>4</sub> + CNT and Mn<sub>3</sub>O<sub>4</sub> + CNF catalysts and the state-of-the-art Pt/C. The two catalysts showed almost similar diffusion current response at *ca* -3.5 mA cm<sup>-2</sup> with half-wave potential ( $E_{1/2}$ ) of *ca*. 0.80 V compared to the Pt/C of  $E_{1/2}$  = 0.86 V.

Considering the comparative performance of the two Mn<sub>3</sub>O<sub>4</sub>-based catalysts toward ORR, RDE experiments were conducted in oxygen-saturated 1.0 M KOH electrolyte at rotating speeds between 400 and 3200 rpm (Figure 4C,D). The number of electrons transferred during the ORR electrocatalytic process was determined using the Koutecky–Levich (K–L) plots in Figure 4E,F, equation (eq 4)<sup>48</sup>

$$\frac{1}{j} = \frac{1}{j^d} + \frac{1}{j^k} = \frac{1}{0.21nFD^{2/3}\gamma - \frac{1}{6}CO_2\omega^{1/2}} + \frac{1}{nFkCO_2} \quad (4)$$

where  $j$  is the measured current,  $j^d$  is the diffusion-limiting current,  $j^k$  is the kinetic current,  $n$  is the number of electrons transferred,  $F$  is the Faraday constant,  $D$  is the diffusion coefficient ( $1.95 \times 10^{-5}$  cm<sup>2</sup> s<sup>-1</sup>),  $\gamma$  is the kinematic viscosity ( $8.98 \times 10^{-3}$  cm<sup>2</sup> s<sup>-1</sup>), CO<sub>2</sub> is the oxygen concentration ( $1.15 \times 10^{-3}$  mol dm<sup>-3</sup>),  $\omega$  is the rotation speed, and  $k$  is the kinetic rate constant. From the slope of the K–L plot in Figure 4E,F the number of electrons transferred during the ORR process using Mn<sub>3</sub>O<sub>4</sub> + CNF and Mn<sub>3</sub>O<sub>4</sub> + CNT as electrocatalysts were 3.87 and 3.98, respectively, approximately 4-electron pathway for the ORR mechanism on the surfaces of Mn<sub>3</sub>O<sub>4</sub> + CNT and Mn<sub>3</sub>O<sub>4</sub> + CNF.

From the results mentioned above, the composites revealed good ORR performance, ascribable to several factors. First, the uniform 1D carbon nanofibrous conductive materials employed as the conductive additive could facilitate electron transport.<sup>49</sup> Second, the greater degrees of graphitization in the carbon matrix with respect to amorphous carbon have the potential to increase electrical conductivity, enabling enhanced ORR catalytic activity.<sup>50,51</sup> Third, increased porosity and surface area of the composite materials can significantly reduce mass transport resistance while increasing the exposed ORR active sites, hence increasing utilization efficiency.<sup>52</sup> Lastly, the synergistic effect between Mn<sub>3</sub>O<sub>4</sub> and carbon matrices can effectively influence the comparatively good ORR performance through enhanced charge transfer kinetics coupled to adsorbents transport during ORR.<sup>48,52,53</sup> Interestingly, both CNTs and CNFs gave almost the same performance for ORR (Table 1). Although Mn<sub>3</sub>O<sub>4</sub> + CNT exhibits higher ECSA

than the Mn<sub>3</sub>O<sub>4</sub> + CNF (Table 1) to enhance electrocatalysis, it seems that such inherent advantage of the CNTs might have been canceled or equalized by the high defects and presence of N in the structure of the CNFs.

The voltammograms (Figure 4G) compare the OER performance of the composite electrocatalysts as well as of the standard IrO<sub>2</sub>. A good bifunctional OER electrocatalyst with good OER kinetics, among other kinetic parameters, should show more negatively shifted potential for the OER onset at the potential at 10 mA cm<sup>-2</sup> ( $j_{=10}$ ). From Figure 4G, Mn<sub>3</sub>O<sub>4</sub> + CNF revealed both the onset and potentials at  $j_{=10}$  of 1.49 and 1.58 V vs RHE respectively, with the peak current density at 71.60 mA cm<sup>-2</sup>. Similarly, Mn<sub>3</sub>O<sub>4</sub> + CNT revealed both onset and benchmark potential at  $j_{=10}$  of 1.50 and 1.59 V vs RHE respectively with the peak current density at 47.49 mA cm<sup>-2</sup>. The obtained OER kinetic parameters and current density are comparable to that of the standard IrO<sub>2</sub> which revealed onset and potentials at  $j = 10$  values of 1.48 and 1.61 V versus RHE respectively and a current density of 68.48 mA cm<sup>-2</sup>. The superior OER performance for Mn<sub>3</sub>O<sub>4</sub> + CNF could be ascribed to the presence of nitrogen on polyacrylonitrile precursor for the CNF; it is known that nitrogen-related species endows more OER active sites.<sup>54</sup> The atoms of carbon adjacent to the atoms of nitrogen are electron-starved, hence are positively charged since the more electronegative nitrogen exerts an undue electron-withdrawing effect in the carbon  $\pi$  system,<sup>54</sup> the positive charge around the carbon makes it easier for OH<sup>-</sup> adsorption on the surface. Other factors include that the positive charge around nitrogen during OER can support the easy recombination of two adsorbed oxygen species O<sub>ads</sub><sup>52,54</sup> plus during OER, as the density of state of nitrogen in a graphitic sp<sup>2</sup> carbon network increases, nitrogen species can participate in the electrocatalytic process.<sup>54,55</sup>

Table 2 compares the ORR and OER kinetic parameters of the as-synthesized electrocatalysts to those from the literature. The overvoltage  $\Delta E$  ( $E_{ORR} - E_{OER}$ ) for the OER and ORR, an indicator of catalytic inefficiency and an important parameter that reveals the least energy required to kick-start the bifunctional ORR and OER electrocatalysis, smaller values are an indication of an effective electrocatalyst. The potential around 10 mA cm<sup>-2</sup> has been known to be the benchmark potential for assessing the viability of an OER catalyst while the half-wave potential ( $E_{1/2}$ ) has been proposed for the viability of an ORR catalyst.<sup>56</sup> The obtained values for Mn<sub>3</sub>O<sub>4</sub> + CNF and Mn<sub>3</sub>O<sub>4</sub> + CNT are (0.79 and 0.80 V vs RHE) respectively. The relatively low overvoltage between the OER and ORR further explains that the bifunctional character exhibited by Mn<sub>3</sub>O<sub>4</sub> + CNF and Mn<sub>3</sub>O<sub>4</sub> + CNT can be attributed to the synergy between the carbon conducting agents and hausmannite Mn<sub>3</sub>O<sub>4</sub>, coupled with the high surface area and presence of electronegative nitrogen on the CNF polyacrylonitrile precursor.

Tafel slope value gives insights into the morphology of an electrocatalyst which has a direct effect on kinetics and



subsequent catalytic activity. The Tafel slopes were obtained from ORR Tafel plots (Figure 4H), and the Tafel slopes recorded for  $\text{Mn}_3\text{O}_4 + \text{CNT}$  and  $\text{Mn}_3\text{O}_4 + \text{CNF}$  composite electrocatalysts are 94 and 79  $\text{mV dec}^{-1}$  respectively. The obtained Tafel slopes from  $\text{Mn}_3\text{O}_4 + \text{CNT}$  and  $\text{Mn}_3\text{O}_4 + \text{CNF}$  are both superior to that of the 20 wt % Pt/C (102  $\text{mV dec}^{-1}$ ). The relatively smaller Tafel slope values for  $\text{Mn}_3\text{O}_4 + \text{CNF}$  and  $\text{Mn}_3\text{O}_4 + \text{CNT}$  as shown in Table 2, is an indication of a slow increase in overpotential with respect to current density, an important parameter for practical applications for fuel cells and RZABs.<sup>56</sup> Also Tafel plots data was obtained from OER voltammograms (Figure 4I), the Tafel slopes recorded for  $\text{Mn}_3\text{O}_4 + \text{CNT}$  and  $\text{Mn}_3\text{O}_4 + \text{CNF}$  composite electrocatalysts are 93 and 85  $\text{mV dec}^{-1}$  respectively while that of  $\text{IrO}_2$  standard is 80  $\text{mV dec}^{-1}$ . Tafel slope shows that  $\text{Mn}_3\text{O}_4 + \text{CNF}$  shows enhanced kinetics compared to its  $\text{Mn}_3\text{O}_4 + \text{CNT}$  counterpart. EIS data of the two electrocatalysts conducted at 1.59 V vs RHE (Figure S7 and Table S2) show that the charge-transfer resistance ( $R_{\text{ct}}$ ) of the  $\text{Mn}_3\text{O}_4 + \text{CNF}$  (149  $\Omega$ ) is smaller than that of the  $\text{Mn}_3\text{O}_4 + \text{CNT}$  (184.6  $\Omega$ ), corroborating the faster kinetics or small Tafel slope value of the  $\text{Mn}_3\text{O}_4 + \text{CNF}$ .

**3.4. Electrocatalytic Stability.** The stability of the catalyst materials for ORR was tested by running 5000 cyclic voltammograms at the scan rate of 50  $\text{mV s}^{-1}$  in 1.0 M KOH electrolyte solution, afterward the ORR voltammograms are repeated at 1600 rpm and the results are shown in Figure S8A,B.  $\text{Mn}_3\text{O}_4 + \text{CNF}$  showed better stability compared to  $\text{Mn}_3\text{O}_4 + \text{CNT}$  with respect to fewer changes in their ORR kinetic parameters. The stability of the OER was ascertained after running a chronopotentiometry experiment at 10  $\text{mA cm}^{-2}$  for 10 h (Figures S8E). Herein, both RDE rotation speed and current density were fixed at 1600 rpm and 10  $\text{mA cm}^{-2}$  for a 10 h period, respectively, while the operating voltage is recorded. The OER voltammograms before and after 10 h chronopotentiometry tests are presented in Figure S8E. Looking at the ORR and OER performance of the electrocatalysts,  $\text{Mn}_3\text{O}_4 + \text{CNF}$  has better bifunctional electrocatalytic performance than its  $\text{Mn}_3\text{O}_4 + \text{CNT}$  counterpart. In general, mass transport is different from electron transport,<sup>57</sup> it is evident that while CNT provides better mass transport features (see Table 1), CNF provides better electron transfer kinetics (see Table 2).

**3.5. Computational Studies.** DFT calculations were undertaken to enable in-depth studies and decipher the extent of adsorption of the ORR and OER intermediates (i.e.,  $\text{O}^*$ ,  $\text{OH}^*$ , and  $\text{OOH}^*$ ). Tubular-type model was chosen for the CNT while fishbone-type (or stacked-cup) model was chosen for the CNF, while the prominent XRD peaks, (211) and (002), were chosen as the model electrode surface (Figure S9). In the DFT calculation, the energy needed for adsorption,  $E_{\text{ad}}$  (eV), is given by (eq 5)

$$E_{\text{ad}} = (E_{\text{surface+adsorbate}}) - (E_{\text{surface}} + E_{\text{adsorbate}}) \quad (5)$$

where  $E_{\text{surface}} + E_{\text{adsorbate}}$  represent the energies of the bare electrode surface and the free adsorbate in the gas phase, respectively. Hence, an increased, negative  $E_{\text{ad}}$  value (i.e., a more exothermic process) signifies stronger adsorption. For ORR/OER processes, however, weak adsorption of the intermediates equates to efficient electrocatalytic performance. Table 3 is a summary of the DFT calculations for the  $\Delta G$ , adsorption energy ( $E_{\text{ad}}$ ) and p-band centre (eV). In all cases, the  $E_{\text{ad}}$  values of the three adsorbed species on the CNF are

**Table 3. DFT Calculated Parameters for the Adsorption of the ORR and the OER Intermediates onto the CNT- and CNF-Based Electrode Surfaces<sup>a</sup>**

electrode	adsorbate	$\Delta G$ (eV)	$E_{\text{ad}}$ (eV)	p-band center (eV)
$\text{Mn}_3\text{O}_4 + \text{CNF}$	$\text{O}^*$	-0.369	-0.369	-6.475
	$\text{OH}^*$	-0.929	-8.959	-1.609
	$\text{OOH}^*$	3.475	-26.136	-1.656
$\text{Mn}_3\text{O}_4 + \text{CNT}$	$\text{O}^*$	-1.214	-1.214	-0.350
	$\text{OH}^*$	-3.361	-11.390	-0.396
	$\text{OOH}^*$	3.233	-26.378	-0.463

<sup>a</sup> $\Delta G$  = Gibbs free energy;  $E_{\text{ad}}$  = Adsorption energy.

weaker than those on the CNT surfaces, suggesting that CNF-based electrodes provide the most preferred electrode surface for the ORR and OER.

Next, an in-depth understanding of the electronic properties of the electrodes was investigated by performing calculations on the electronic band structures and the projected density of states (PDOS) (exemplified in Figure 5 with an adsorption of  $\text{O}^*$ ). The results show that band structures (Figure 5 A(i),B(i) for  $\text{O}^*$ -adsorbed on the CNF and CNT, respectively) are essentially similar. However, their PDOS differ as evident in Figure 5A(ii),B(ii) where the PDOS value is up to 67 eV for the CNF and only about 51 eV for the CNT, implying presence of more electrons/eV for CNF with  $\text{O}^*$  as adsorbate (i.e., increased conductivity). Also, the d-electrons from the Mn (represented in blue color) are more distributed in the CNF than in the CNT, which indicates more participation of the Mn in the electronic processes in the CNF surface than in the CNT surface. The same finding was observed for the intermediate,  $\text{OH}^*$  and  $\text{OOH}^*$  (Figure S10). In summary, the increased electron density and efficient participation of the Mn d-electrons in the CNF-based electrode bode well for efficient electrocatalysis of the ORR and the OER.

From the PDOS (Figure 5), the p-band dominates the s- and d-bands due to the presence of the organic/carbon support. The interaction of the ORR/OER species on the  $\text{Mn}_3\text{O}_4$  surface was further proved by the p-band center ( $\epsilon_p$ ) of PDOS (Figure S11). As summarized on Table 3, the calculated p-band centers upon the interaction of the  $\text{O}^*$ ,  $\text{OH}^*$ , and  $\text{OOH}^*$  with the  $\text{Mn}_3\text{O}_4 + \text{CNF}$  are far away from the Fermi level than with the  $\text{Mn}_3\text{O}_4 + \text{CNT}$ , which suggests that weaker interactions of the ORR/OER intermediates with the  $\text{Mn}_3\text{O}_4 + \text{CNF}$  catalyst. This result agrees with the data on the adsorption energy (Table 3) and the interpretation thereof.

### 3.6. Rechargeable Zinc–Air Battery Performance.

Considering the high performance of the  $\text{Mn}_3\text{O}_4 + \text{CNF}$ , both experimental (in terms of electron transfer kinetics) and theory (based on DFT data) over its  $\text{Mn}_3\text{O}_4 + \text{CNT}$  counterparts toward ORR/OER activities,  $\text{Mn}_3\text{O}_4 + \text{CNF}$  was chosen to study for the full-cell RZAB, summarized in Figure 6. As shown in Figure 6A,  $\text{Mn}_3\text{O}_4 + \text{CNF}$  and state-of-the-art catalysts (Pt/C– $\text{IrO}_2$ ) showed essentially the same bifunctionality values ( $\Delta E \approx 0.78\text{--}0.8$  V). The power density (Figure 6B) of the Pt/C– $\text{IrO}_2$  (ca. 215  $\text{mW cm}^{-2}$ ) is higher than that of the  $\text{Mn}_3\text{O}_4 + \text{CNF}$  (ca. 178  $\text{mW cm}^{-2}$ ) but, as will be shown later, the  $\text{Mn}_3\text{O}_4 + \text{CNF}$  exhibits superior performance than the Pt/C– $\text{IrO}_2$ . The 3D micro-RZAB cell exhibited an excellent open-circuit voltage of 1.77 V and could light up a 1.6 V LED bulb (Figure 6C). The most important property of RZAB is its areal-discharge energy density ( $\text{mW h cm}_{\text{geometric}}^{-2}$ ). Thus, for any claim of real technological

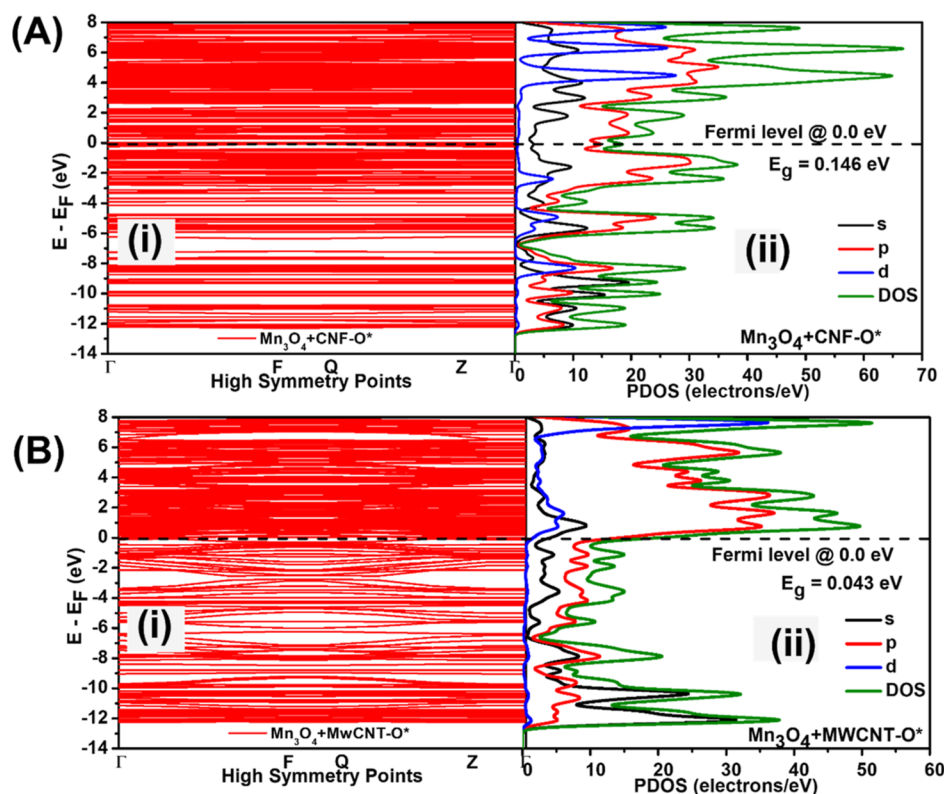


**Figure 5.** Typical band structures (A(i) and B(i)) and PDOS (A(ii) and B(ii)) for \*O adsorbed on CNF (A) and CNT electrodes. Unlike the MWCNTs, PDOS suggests that CNF allows for the participation of the d-electron from  $\text{Mn}_3\text{O}_4$  (compare the blue waves). This is the reason for the favorable adsorption of the oxygen intermediates for efficient electrocatalysis.

breakthrough in RZAB, laboratory researchers have been urged to focus on deep-cycling (i.e., long-hour discharge cycling) rather than the extremely superficial or shallow cycling (few seconds or minutes' discharge cycling) that characterizes most publications in RZAB today. Shallow cycling is not a technological breakthrough, as it cannot compete with the conventional Li-ion battery. It is for this reason that Rolison and co-workers,<sup>9</sup> stated that “to compete with Li-ion batteries, researchers should cycle zinc–air cells at  $35 \text{ mW h cm}_{\text{geometric}}^{-2}$ ” (which maps to a Li-Ion pack-level specific energy of  $120 \text{ W h kg}_{\text{pack}}^{-1}$ ) and, preferably, at the technological currently loading of  $10 \text{ mA cm}^{-2}$ .<sup>10</sup>

Motivated by the need to comply with the above recommended standard, this work subjected the RZAB cells to long-hour discharge–charge cycles. Figure 6D exemplifies discharge–charge cycling of 16 h per cycle (i.e., 8 h discharge, 8 h charge) at a current loading of  $5 \text{ mA cm}^{-2}$ , comparing both  $\text{Mn}_3\text{O}_4 + \text{CNF}$  and  $\text{Pt/C-IrO}_2$  as air-catalysts. The findings here should be emphasized. First, within the first 10 cycles ( $\sim 150 \text{ h}$ ), the  $\text{Mn}_3\text{O}_4 + \text{CNF}$  showed better kinetics/bifunctionality ( $\Delta E = 0.8 \text{ V}$ ) and areal-discharge energy density (at  $48 \text{ mW h cm}_{\text{geometric}}^{-2}$ ) than the precious commercial catalysts ( $\text{Pt/C-IrO}_2$ ) with  $\Delta E = 1.0 \text{ V}$  and areal-discharge energy density of  $40 \text{ mWh cm}_{\text{geometric}}^{-2}$ . Second, while  $\text{Mn}_3\text{O}_4 + \text{CNF}$  is able to maintain its cycling for 270 h with  $\Delta E = 1.0 \text{ V}$  and  $44 \text{ mW h cm}_{\text{geometric}}^{-2}$ , the commercial  $\text{Pt/C-IrO}_2$  could not sustain the RZAB cell for more than 150 h. These findings prove the superiority of  $\text{Mn}_3\text{O}_4 + \text{CNF}$  as an air-catalyst for RZAB over the  $\text{Pt/C-IrO}_2$ .

Further, the RZAB cell was subjected to a technological current loading of  $10 \text{ mA cm}^{-2}$  at 8 h per cycle (i.e., four discharges, 4 h charge) for 25 cycles (240 h). As shown in Figure 6E, it is interesting to observe that at every cycle, the RZAB charged at an average of 1.6 h per cycle, while it discharged at 4 h per cycle, thereby giving a total of 25 cycles for 140 h, with an average discharge voltage of 1.0 V and an areal-discharge energy density of  $40 \text{ mW h cm}^{-2}$ . Table S3 compares 100 recent peer-reviewed articles on RZAB, and only an article with nitrogen-enriched carbon nanospheres catalyst that attained up to  $46 \text{ mW h cm}^{-2}$ .<sup>58</sup> As seen from Table S3, our current work outperformed nearly all of the listed recent literature because these researchers reported only shallow discharge–charge cycles. In addition, continuous long-term discharging (56.5 h) at  $10 \text{ mA cm}^{-2}$  led to a high specific capacity of  $777.8 \text{ mA h g}_{\text{zn}}^{-1}$  with zinc utilization of  $\sim 95\%$  (Figure 6F). Also, rate capability tests showed that  $\text{Mn}_3\text{O}_4 + \text{CNF}$  can be discharged–charged between 5 and  $30 \text{ mA cm}^{-2}$ . These findings are critical, as they suggest that a low-cost Mn-based carbon composite electrocatalyst, if optimized, has the potential to be utilized in technological applications.

To provide some insight into the morphology and/or structural reorganization that would impact the ionic and electronic transport, we adopted EIS to explore the electrochemical performance of the RZAB cell at the beginning-of-life (BoL) and end-of-life (EoL). The Nyquist plots (Figure 7A,B) were satisfactorily fitted with an RC + Randles equivalent electrical circuit (EEC, Figure 7C).

The EEC fitting parameters and values summarized in Table 4 comprise the bulk resistance ( $R_b$ ) which describes resistance arising from the electrodes, electrolytes, current collectors, and

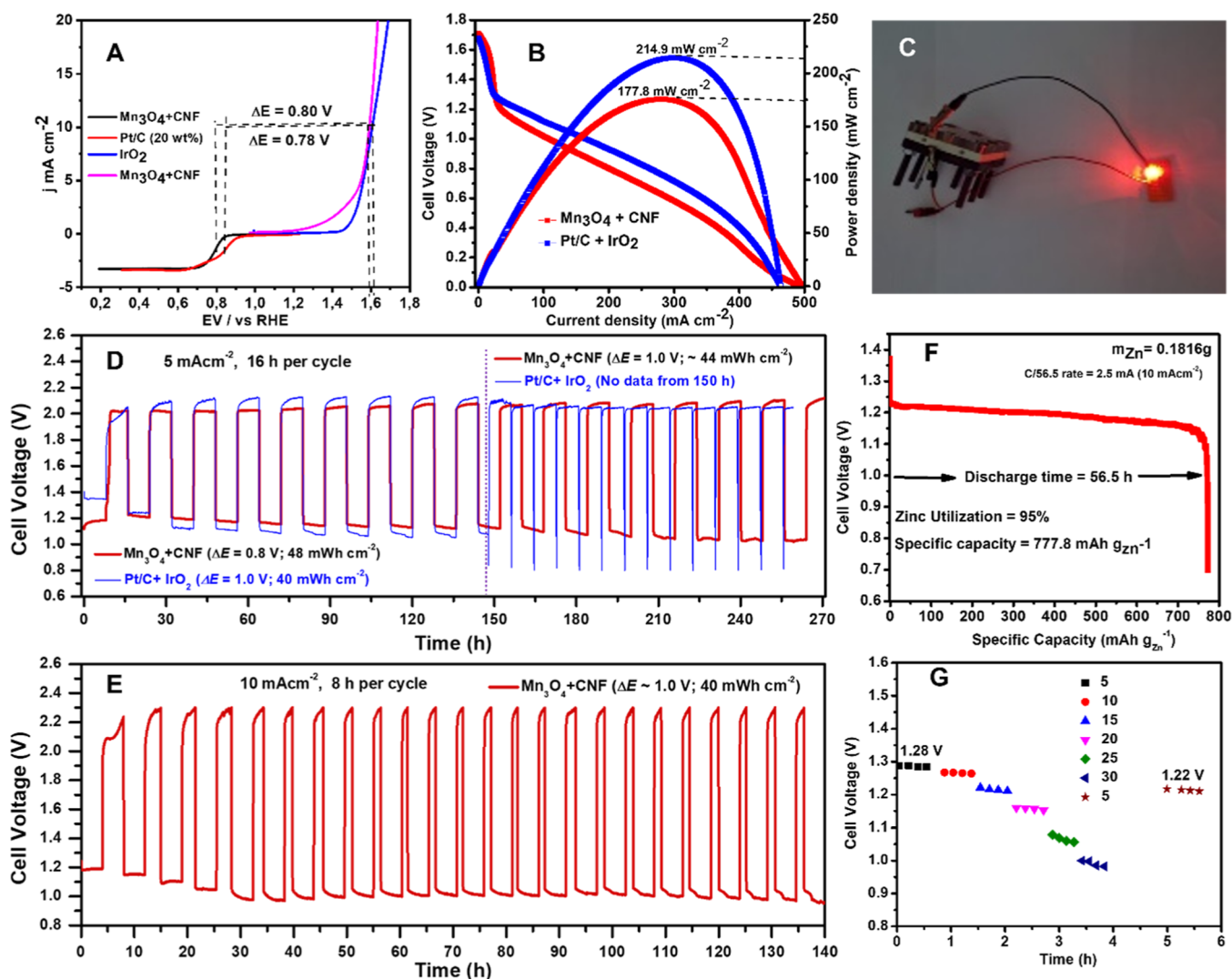


**Figure 6.** (A) Comparative plots of the OER and ORR bifunctional activity at the two  $\text{Mn}_3\text{O}_4$ -based catalysts and state-of-the-art catalysts; (B) plots of power density of  $\text{Mn}_3\text{O}_4 + \text{CNF}$  and  $\text{Pt}/\text{C}$ ; (C) picture of connection of the RZAB with  $\text{Mn}_3\text{O}_4 + \text{CNF}$  air-cathode to light a 1.6 V LED bulb; long-term discharge–charge profiles obtained at (D)  $5 \text{ mA cm}^{-2}$  at 16 h per cycle for  $\text{Mn}_3\text{O}_4 + \text{CNF}$  and  $\text{Pt}/\text{C}/\text{IrO}_2$ , and (E)  $10 \text{ mA cm}^{-2}$  and 8 h per cycle for  $\text{Mn}_3\text{O}_4 + \text{CNF}$ ; (F) long-term discharge of  $\text{Mn}_3\text{O}_4 + \text{CNF}$  at  $10 \text{ mA cm}^{-2}$ ; (G) rate capability of the RZAB at current densities between 5 and  $30 \text{ mA cm}^{-2}$ .

wires; resistance due to surface film ( $R_{\text{sf}}$ ); charge-transfer resistance ( $R_{\text{ct}}$ ), constant-phase elements ( $\text{CPE}_{\text{sf}}$  and  $\text{CPE}_{\text{ct}}$ ) arising from such factors as surface roughness, inhomogeneity in electrode surface terminations, porosity of electrode modifier/catalysts, and complexity in the double-layer structure; and Warburg resistance ( $Z_{\text{W}}$ ) due to diffusion resistance of the Zn-ion.

Before we proceed, it may be necessary to briefly explain the relevance of the impedance arising from the CPE (i.e.,  $Z_{\text{CPE}}$ ). The  $Z_{\text{CPE}}$  is mathematically defined as in eq <sup>6,30,59</sup>

$$Z_{\text{CPE}} = \frac{1}{Q(j\omega)^n} \quad (6)$$

where  $Q$  is the nonideal capacitance ( $j = \sqrt{-1}$ ),  $\omega$  is the radial frequency, and  $n$  is the ideality factor (i.e.,  $-1 \leq n \leq 1$ ).  $Z_{\text{CPE}}$  is described as an ideal resistor if  $n = 0$ , an ideal capacitor if  $n = 1$  (i.e.,  $Q = C$ ), an ideal inductor if  $n = -1$ , and pure diffusion if  $n = 0.5$ . The fitted EIS data for the RZAB cell (BoL and EoL) are summarized in Table 4. The parallel  $R_{\text{sf}}||\text{CPE}_{\text{sf}}$  circuit is associated with the resistance arising from the formation of a

surface film or layer on the electrode with a high-frequency response. Although difficult to observe by visual inspection, the  $R_{\text{sf}}||\text{CPE}_{\text{sf}}$  circuit proved necessary as it was impossible to fit the EIS data in this work without its inclusion in the overall EEC. The parallel  $R_{\text{ct}}||\text{CPE}_{\text{ct}}$  circuit is associated with the charge transfer (Faradaic process) and its accompanying CPE (non-Faradaic process) at the medium frequency region, while the  $Z_{\text{W}}$  occurs at the low frequency region.

From the results,  $R_{\text{b}}$  values increased by 45% at EoL (i.e., 4.26 to  $6.18 \Omega$ ). The  $R_{\text{sf}}$  which is the resistance of Zn-ion migration through the surface film increased by about 154% at EoL (i.e., 1.22 to  $3.10 \Omega$ , or ca. 0.01% growth per minute), meaning that the growth of such surface films over the extended long-hour discharge–charge cycles leads to higher resistance. The associated  $\text{CPE}_{\text{sf}}$  decreased by about 22% (i.e., from 180 to  $40 \text{ mFs}^{(n-1)}$ ) which means that the surface films transformed from a rough/porous to a less porous and smoother surface upon longer cycling. This is corroborated by the  $n_{\text{sf}}$  value that decreased by about 26%, changing from 0.76 (mixed Faradaic/non-Faradaic process or pseudocapacitance)

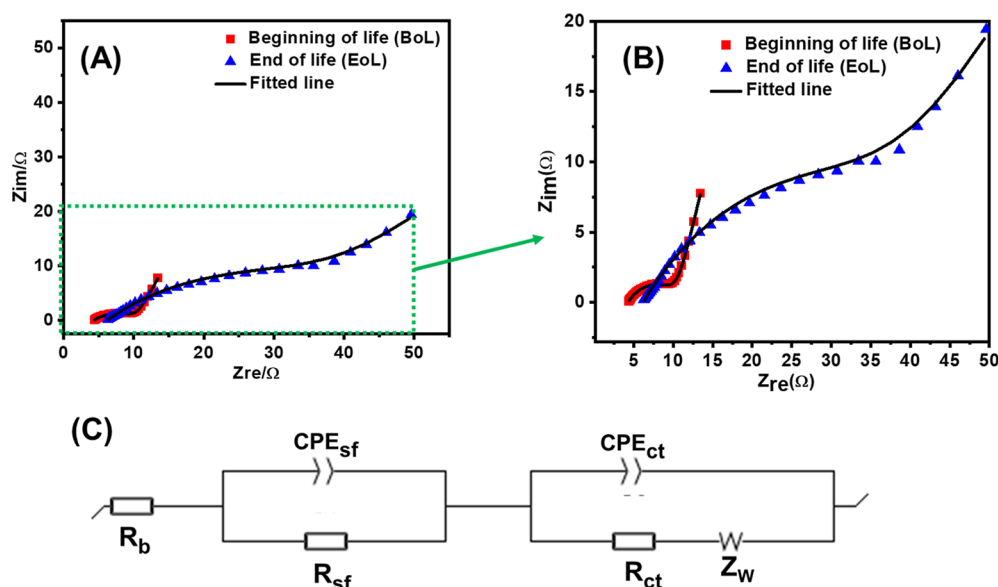


**Figure 7.** (A) Nyquist plots of the RZAB cell before (BoL) and after (EoL) the long-term cycling of 270 h (as in Figure 6D), (B) zoomed in Figure 7A for clarity, and (C) RC + Randles' EEC used in fitting the EIS data.

**Table 4. EIS Fitted Results for Fabricated RZAB Using  $\text{Mn}_3\text{O}_4$  + CNF as Air Cathode Catalyst**

EIS fitted parameter	beginning of life (BoL)	end of life (EoL)
$R_b/\Omega$	$4.260 \pm 0.003$	$6.179 \pm 0.020$
$R_{sf}/\Omega$	$1.220 \pm 0.004$	$3.098 \pm 0.090$
$\text{CPE}_{sf}/F \text{ s}^{(n-1)}$	$0.180 \pm 0.790$	$0.040 \pm 0.005$
$n_{sf}$	$0.760 \pm 0.003$	$0.960 \pm 0.003$
$R_{ct}/\Omega$	$6.540 \pm 0.030$	$39.800 \pm 0.830$
$\text{CPE}_{ct}/F \text{ s}^{(n-1)}$	$0.010 \pm 0.003$	$0.005 \pm 0.006$
$n_{ct}$	$0.450 \pm 0.002$	$0.480 \pm 0.001$
$Z_w/\Omega \text{ s}^{-1/2}$	$1.240 \pm 0.780$	$14.200 \pm 0.740$

to 0.96 (which is close to unity or ideal capacitance). At the midfrequency region, the  $R_{ct}$  increased by about 509% (i.e., from 6.54 to 39.80  $\Omega$ ), explaining the slight loss of kinetics ( $\Delta E$  from 0.8 to 1.0 V, Figure 6D). Its  $\text{CPE}_{ct}$  decreased by 50% (i.e., from 10 to 5  $\text{mFs}^{(n-1)}$ ) while the  $n_{ct}$  values (BoL and EoL) remained essentially the same (*ca.* 0.5) suggesting the nonstop occurrence of a pure ionic diffusion process. Finally, the  $Z_w$  value increased from 1.24  $\Omega \text{ s}^{-1/2}$  (BoL) to 14.2  $\Omega \text{ s}^{-1/2}$  (EoL) which further confirms the observed loss of kinetics.

#### 4. CONCLUSIONS

In summary, we were able to successfully synthesize carbon nanomaterials using electrospinning and carbonization techniques for CNFs and the CVD method for CNTs.  $\text{Mn}_3\text{O}_4$  synthesis was achieved successfully by the annealing process using a horizontal furnace. Composite electrocatalysts  $\text{Mn}_3\text{O}_4$  + CNT and  $\text{Mn}_3\text{O}_4$  + CNF were fabricated from the nanomaterials, and their electrocatalytic performance indicators like activity, stability, and electrochemical active surface area were evaluated. Other catalytic efficiency parameters investigated are the catalysts' specific current density per catalyst surface area ( $j_s$ ) and RF.  $\text{Mn}_3\text{O}_4$  + CNF showed better performance ascribable to the PAN employed for nanofiber fabrication as well as provided both the carbon and nitrogen source during pyrolysis, and the presence of nitrogen on the carbon nanofiber had a significant effect in terms of overall bifunctionality as a catalyst. Furthermore, the synergistic

coupling of Mn species and the carbon matrix endows synergistic effect which can improve charge transfer kinetics; adsorbents transport which impacts positively on catalytic activity. Hence, the preparation of  $\text{Mn}_3\text{O}_4$  + CNTs and  $\text{Mn}_3\text{O}_4$  + CNFs with enhanced OER and ORR activity provides alternative electrocatalysts for the all-important oxygen electrochemistry occurring in the air-cathodes of RZABs.  $\text{Mn}_3\text{O}_4$  + CNF was explored as a cathode electrocatalyst for the proof-of-concept in a RZAB employing a two-electrode system and using micro 3D printed cells; the electrolyte medium is composed of 6.0 M KOH and 0.2 M zinc acetate. Assembled battery revealed improved reversibility performance with a change in voltage ( $\Delta E$ ) slightly better to RZAB with Pt/C (20 wt %) +  $\text{IrO}_2$  as air-cathode. The fabricated RZAB revealed a good discharge profile with a specific capacity of about 777.8  $\text{mA h g}_{\text{zn}}^{-1}$  at 10  $\text{mA cm}^{-2}$ . Furthermore, RZAB with  $\text{Mn}_3\text{O}_4$  + CNF as air-cathode was able to undergo discharge/charge cycles at 5  $\text{mA cm}^{-2}$  for 16 h per cycle for over 170 h whereas the RZAB with Pt/C (20 wt %) +  $\text{IrO}_2$  crashed after 140 h under similar conditions. The fabricated RZAB when connected lit a 1.6 V LED bulb for over 5 h before reduction in brightness of the bulb in practical application. This research demonstrates the potential of the manganese carbon composite electrocatalysts as highly active materials for bifunctional air-cathode electrocatalysis of oxygen for energy storage and conversion devices.

#### ASSOCIATED CONTENT

##### Supporting Information

The Supporting Information is available free of charge at <https://pubs.acs.org/doi/10.1021/acsomega.4c05968>.

Synthesis scheme for  $\text{Mn}_3\text{O}_4$  from EMD and corresponding SEM images, EDS, BET/Nitrogen adsorption/desorption curves and XPS Survey spectra. Measurements of double-layer capacitance to determine the ECSA, EIS data, CV and RDE for long-term cycling tests, including chronoamperograms at 10  $\text{mA cm}^{-2}$  for 10 h. Description of the DFT modeling procedure and schematics for the adsorption of ORR/OER intermedi-

ates, band structures, PDOS and p-band centers. Tables showing BET properties, EIS fitted data, and survey of 100 recent literature (including this work) on rechargeable zinc-air batteries showing how this work outperforms most literature, especially in terms of areal-discharge energy density (PDF)

## AUTHOR INFORMATION

### Corresponding Author

**Kenneth I. Ozoemena** – Molecular Sciences Institute, School of Chemistry, University of the Witwatersrand, Johannesburg 2050, South Africa; [orcid.org/0000-0001-7107-7003](https://orcid.org/0000-0001-7107-7003); Email: [Kenneth.ozoemena@wits.ac.za](mailto:Kenneth.ozoemena@wits.ac.za)

### Authors

**Augustus K. Lebechi** – Molecular Sciences Institute, School of Chemistry, University of the Witwatersrand, Johannesburg 2050, South Africa

**Lesego Gaolathe** – Molecular Sciences Institute, School of Chemistry, University of the Witwatersrand, Johannesburg 2050, South Africa

**Thapelo P. Mofokeng** – Molecular Sciences Institute, School of Chemistry, University of the Witwatersrand, Johannesburg 2050, South Africa

**Aderemi B. Haruna** – Molecular Sciences Institute, School of Chemistry, University of the Witwatersrand, Johannesburg 2050, South Africa

**Adewale K. Ipadeola** – Molecular Sciences Institute, School of Chemistry, University of the Witwatersrand, Johannesburg 2050, South Africa; Present Address: Center for advanced materials, Qatar University, Doha 2713, Qatar; [orcid.org/0000-0001-8896-6763](https://orcid.org/0000-0001-8896-6763)

**Patrick V. Mwonga** – Molecular Sciences Institute, School of Chemistry, University of the Witwatersrand, Johannesburg 2050, South Africa

**Oluwatosin E. Bankole** – Molecular Sciences Institute, School of Chemistry, University of the Witwatersrand, Johannesburg 2050, South Africa; Present Address: School of Science and Technology, Babcock University, Ilisan-Remo, Ogun State, Nigeria.

**Oluwafunmilola Ola** – Advanced Materials Group, Faculty of Engineering, the University of Nottingham, Nottingham NG7 2RD, U.K.

Complete contact information is available at:

<https://pubs.acs.org/10.1021/acsomega.4c05968>

### Notes

The authors declare no competing financial interest.

## ACKNOWLEDGMENTS

The authors are grateful for the financial support of the National Foundation of Research (NRF), the Department of Science and Innovation (DSI) Energy Storage Consortium, and the DSI-NRF-Wits SARChI Chair in Materials Electrochemistry and Energy Technologies (MEET) (UID no.: 132739), and the Royal Society for the International collaboration award (ICAO\R1\231033-ISPF). We thank the Centre for High Performance Computing (CHPC, Cape Town, South Africa) for granting us unrestricted access to the computing facilities for DFT calculations.

## REFERENCES

- (1) Li, Y.; Gong, M.; Liang, Y.; Feng, J.; Kim, J.-E.; Wang, H.; Hong, G.; Zhang, B.; Dai, H. Advanced zinc-air batteries based on high-performance hybrid electrocatalysts. *Nat. Commun.* **2013**, *4* (1), 1805.
- (2) Li, Y.; Dai, H. Recent advances in zinc-air batteries. *Chem. Soc. Rev.* **2014**, *43* (15), 5257–5275.
- (3) Pei, P.; Wang, K.; Ma, Z. Technologies for extending zinc-air battery's cyclelife: A review. *Appl. Energy* **2014**, *128*, 315–324.
- (4) Ipadeola, A. K.; Haruna, A. B.; Gaolathe, L.; Lebechi, A. K.; Meng, J.; Pang, Q.; Eid, K.; Abdullah, A. M.; Ozoemena, K. I. Efforts at Enhancing Bifunctional Electrocatalysis and Related Events for Rechargeable Zinc-Air Batteries. *ChemElectroChem* **2021**, *8* (21), 3998–4018.
- (5) Wang, M.; Qian, T.; Zhou, J.; Yan, C. An efficient bifunctional electrocatalyst for a zinc-air battery derived from Fe/N/C and bimetallic metal-organic framework composites. *ACS Appl. Mater. Interfaces* **2017**, *9* (6), 5213–5221.
- (6) Chen, W.; Huang, J.; Wei, J.; Zhou, D.; Cai, J.; He, Z.-D.; Chen, Y.-X. Origins of high onset overpotential of oxygen reduction reaction at Pt-based electrocatalysts: A mini review. *Electrochem. Commun.* **2018**, *96*, 71–76.
- (7) Appel, A. M.; Helm, M. L. Determining the overpotential for a molecular electrocatalyst. *ACS Catal.* **2014**, *4*, 630–633.
- (8) Huang, Z. F.; Wang, J.; Peng, Y.; Jung, C. Y.; Fisher, A.; Wang, X. Design of efficient bifunctional oxygen reduction/evolution electrocatalyst: recent advances and perspectives. *Adv. Energy Mater.* **2017**, *7* (23), 1700544.
- (9) Hopkins, B. J.; Chervin, C. N.; Parker, J. F.; Long, J. W.; Rolison, D. R. An areal-energy standard to validate air-breathing electrodes for rechargeable zinc-air batteries. *Adv. Energy Mater.* **2020**, *10* (30), 2001287.
- (10) Gallagher, K. G.; Goebel, S.; Greszler, T.; Mathias, M.; Oelerich, W.; Eroglu, D.; Srinivasan, V. Quantifying the promise of lithium-air batteries for electric vehicles. *Energy Environ. Sci.* **2014**, *7* (5), 1555–1563.
- (11) Shang, C.; Yang, M.; Wang, Z.; Li, M.; Liu, M.; Zhu, J.; Zhu, Y.; Zhou, L.; Cheng, H.; Gu, Y.; et al. Encapsulated MnO in N-doping carbon nanofibers as efficient ORR electrocatalysts. *Sci. China Mater.* **2017**, *60* (10), 937–946.
- (12) Fu, J.; Cano, Z. P.; Park, M. G.; Yu, A.; Fowler, M.; Chen, Z. Electrically rechargeable zinc-air batteries: progress, challenges, and perspectives. *Adv. Mater.* **2017**, *29* (7), 1604685.
- (13) Blurton, K. F.; Sammells, A. F. Metal/air batteries: their status and potential—a review. *J. Power Sources* **1979**, *4* (4), 263–279.
- (14) Yu, Y.; Zuo, Y.; Liu, Y.; Wu, Y.; Zhang, Z.; Cao, Q.; Zuo, C. Directly electrospun carbon nanofibers incorporated with MN3O4 nanoparticles as bending-resistant cathode for flexible al-air batteries. *Nanomaterials* **2020**, *10* (2), 216.
- (15) Li, L.; Yang, J.; Yang, H.; Zhang, L.; Shao, J.; Huang, W.; Liu, B.; Dong, X. Anchoring Mn3O4 nanoparticles on oxygen functionalized carbon nanotubes as bifunctional catalyst for rechargeable zinc-air battery. *ACS Appl. Energy Mater.* **2018**, *1* (3), 963–969.
- (16) Dong, M.; Liu, X.; Jiang, L.; Zhu, Z.; Shu, Y.; Chen, S.; Dou, Y.; Liu, P.; Yin, H.; Zhao, H. Cobalt-doped Mn3O4 nanocrystals embedded in graphene nanosheets as a high-performance bifunctional oxygen electrocatalyst for rechargeable Zn-Air batteries. *Green Energy Environ.* **2020**, *5* (4), 499–505.
- (17) Ejikeme, P. M.; Makgopa, K.; Ozoemena, K. I. Effects of catalyst-support materials on the performance of fuel cells. In *Nanomater. for Fuel Cell Catal.*; Springer, 2016; pp 517–550.
- (18) Chang, H.; Liu, X.; Zhao, S.; Liu, Z.; Lv, R.; Zhang, Q.; Yi, T. F. Self-Assembled 3D N/P/S-Tridoped Carbon Nanoflower with Highly Branched Carbon Nanotubes as Efficient Bifunctional Oxygen Electrocatalyst Toward High-Performance Rechargeable Zn-Air Batteries. *Adv. Funct. Mater.* **2023**, *34*, 2313491.
- (19) Tetana, Z.; Mhlanga, S.; Bepete, G.; Krause, R.; Coville, N. The synthesis of nitrogen-doped multiwalled carbon nanotubes using an Fe-Co/CaCO3 catalyst. *S. Afr. J. Chem.* **2012**, *65*, 39–49.

- (20) Ibrahim, S. O.; Mohammed, K. I.; Abubakar, A. A.; Kasim, I. U.; Abdulkareem, A. S. *Synthesis and Characterization of Carbon Nanotubes over Binary Fe-Co-CaCO<sub>3</sub> Catalyst*; Petroleum Technology Development Journal, 2024.
- (21) Mhlanga, S. D.; Mondal, K. C.; Carter, R.; Witcomb, M. J.; Coville, N. J. The effect of synthesis parameters on the catalytic synthesis of multiwalled carbon nanotubes using Fe-Co/CaCO<sub>3</sub> catalysts. *S. Afr. J. Chem.* **2009**, *62*, 67–76.
- (22) Ipadeola, A. K.; Lisa Mathebula, N. Z.; Pagliaro, M. V.; Miller, H. A.; Vizza, F.; Davies, V.; Jia, Q.; Marken, F.; Ozoemena, K. I. Unmasking the Latent Passivating Roles of Ni (OH)<sub>2</sub> on the Performance of Pd-Ni Electrocatalysts for Alkaline Ethanol Fuel Cells. *ACS Appl. Energy Mater.* **2020**, *3* (9), 8786–8802.
- (23) Song, M. J.; Kim, I. T.; Kim, Y. B.; Shin, M. W. Self-standing, binder-free electrospun Co<sub>3</sub>O<sub>4</sub>/carbon nanofiber composites for non-aqueous Li-air batteries. *Electrochim. Acta* **2015**, *182*, 289–296.
- (24) Du, J.; Gao, Y.; Chai, L.; Zou, G.; Li, Y.; Qian, Y. Hausmannite Mn<sub>3</sub>O<sub>4</sub> nanorods: synthesis, characterization and magnetic properties. *Nanotechnology* **2006**, *17* (19), 4923–4928.
- (25) Masipa, P. M.; Magadzhu, T.; Mkhondo, B. Decoration of multiwalled carbon nanotubes by metal nanoparticles and metal oxides using chemical evaporation method. *S. Afr. J. Chem.* **2013**, *66*, 173–178.
- (26) Batakliiev, T.; Petrova-Doycheva, I.; Angelov, V.; Georgiev, V.; Ivanov, E.; Kotsilkova, R.; Casa, M.; Cirillo, C.; Adami, R.; Sarno, M.; et al. Effects of graphene nanoplatelets and multiwall carbon nanotubes on the structure and mechanical properties of poly (lactic acid) composites: a comparative study. *Appl. Sci.* **2019**, *9* (3), 469.
- (27) Makgopa, K.; Raju, K.; Ejikeme, P. M.; Ozoemena, K. I. High-performance Mn<sub>3</sub>O<sub>4</sub>/onion-like carbon (OLC) nanohybrid pseudo-capacitor: Unravelling the intrinsic properties of OLC against other carbon supports. *Carbon* **2017**, *117*, 20–32.
- (28) Rosaiah, P.; Zhu, J.; Hussain, O.; Qiu, Y. Synthesis of flower-like reduced graphene oxide-Mn<sub>3</sub>O<sub>4</sub> nanocomposite electrodes for supercapacitors. *Appl. Phys. A: Mater. Sci. Process.* **2018**, *124* (9), 597.
- (29) Nagamuthu, S.; Vijayakumar, S.; Muralidharan, G. Synthesis of Mn<sub>3</sub>O<sub>4</sub>/amorphous carbon nanoparticles as electrode material for high performance supercapacitor applications. *Energy Fuels* **2013**, *27* (6), 3508–3515.
- (30) Mofokeng, T. P.; Ipadeola, A. K.; Tetana, Z. N.; Ozoemena, K. I. Defect-engineered nanostructured Ni/MOF-derived carbons for an efficient aqueous battery-type energy storage device. *ACS Omega* **2020**, *5* (32), 20461–20472.
- (31) Xu, Y.; Zhang, C.; Zhou, M.; Fu, Q.; Zhao, C.; Wu, M.; Lei, Y. Highly nitrogen doped carbon nanofibers with superior rate capability and cyclability for potassium ion batteries. *Nat. Commun.* **2018**, *9* (1), 1720.
- (32) Zhao, J.; Chen, J.; Xu, S.; Shao, M.; Zhang, Q.; Wei, F.; Ma, J.; Wei, M.; Evans, D. G.; Duan, X. Hierarchical NiMn layered double hydroxide/carbon nanotubes architecture with superb energy density for flexible supercapacitors. *Adv. Funct. Mater.* **2014**, *24* (20), 2938–2946.
- (33) Li, J.; Zhang, W.; Zhang, X.; Huo, L.; Liang, J.; Wu, L.; Liu, Y.; Gao, J.; Pang, H.; Xue, H. Copolymer derived micro/meso-porous carbon nanofibers with vacancy-type defects for high-performance supercapacitors. *J. Mater. Chem. A* **2020**, *8* (5), 2463–2471.
- (34) Zhao, L. Z.; Young, V. XPS studies of carbon supported films formed by the resistive deposition of manganese. *J. Electron Spectrosc. Relat. Phenom.* **1984**, *34* (1), 45–54.
- (35) Carver, J.; Schweitzer, G.; Carlson, T. A. Use of X-ray photoelectron spectroscopy to study bonding in Cr, Mn, Fe, and Co compounds. *J. Chem. Phys.* **1972**, *57* (2), 973–982.
- (36) Deeney, C.; Wang, S.; Belhout, S. A.; Gowen, A.; Rodriguez, B. J.; Redmond, G.; Quinn, S. J. Templated microwave synthesis of luminescent carbon nanofibers. *RSC Adv.* **2018**, *8* (23), 12907–12917.
- (37) Yan, F.; Dong, L.; Su, J.; Liu, X.; Han, X.; Zang, J.; Wang, Y. Copper coordinated with nitrogen in electrospun carbon nanofibers as a high-performance electrocatalyst for ORR. *Electrochem. Commun.* **2022**, *136*, 107245.
- (38) Duan, J.; Chen, S.; Dai, S.; Qiao, S. Z. Shape control of Mn<sub>3</sub>O<sub>4</sub> nanoparticles on nitrogen-doped graphene for enhanced oxygen reduction activity. *Adv. Funct. Mater.* **2014**, *24* (14), 2072–2078.
- (39) Trasatti, S.; Petrii, O. Real surface area measurements in electrochemistry. *J. Electroanal. Chem.* **1992**, *327* (1–2), 353–376.
- (40) Benck, J. D.; Chen, Z.; Kuritzky, L. Y.; Forman, A. J.; Jaramillo, T. F. Amorphous molybdenum sulfide catalysts for electrochemical hydrogen production: insights into the origin of their catalytic activity. *ACS Catal.* **2012**, *2* (9), 1916–1923.
- (41) Iseki, S.; Ohashi, K.; Nagaura, S. Impedance of the oxygen-evolution reaction on noble metal electrodes. *Electrochim. Acta* **1972**, *17* (12), 2249–2265.
- (42) Badawy, W.; Gad-Allah, A.; Abd El-Rahman, H.; Abouromia, M. Kinetics of the passivation of molybdenum in acids and alkali solutions as inferred from impedance and potential measurements. *Surf. Coat. Technol.* **1986**, *27* (2), 187–196.
- (43) Fournier, J.; Brossard, L.; Tilquin, J. Y.; Colté, R.; Dodelet, J.; Guay, D.; Ménard, H. Hydrogen evolution reaction in alkaline solution: Catalytic influence of Pt supported on graphite vs. Pt inclusions in graphite. *J. Electrochem. Soc.* **1996**, *143* (3), 919–926.
- (44) Gasteiger, H. A.; Kocha, S. S.; Sompalli, B.; Wagner, F. T. Activity benchmarks and requirements for Pt, Pt-alloy, and non-Pt oxygen reduction catalysts for PEMFCs. *Appl. Catal., B* **2005**, *56* (1–2), 9–35.
- (45) Suntivich, J.; May, K. J.; Gasteiger, H. A.; Goodenough, J. B.; Shao-Horn, Y. A perovskite oxide optimized for oxygen evolution catalysis from molecular orbital principles. *Science* **2011**, *334* (6061), 1383–1385.
- (46) Walter, M. G.; Warren, E. L.; McKone, J. R.; Boettcher, S. W.; Mi, Q.; Santori, E. A.; Lewis, N. S. Solar water splitting cells. *Chem. Rev.* **2010**, *110* (11), 6446–6473.
- (47) Weber, M. F.; Dignam, M. J. Efficiency of splitting water with semiconducting photoelectrodes. *J. Electrochem. Soc.* **1984**, *131* (6), 1258–1265.
- (48) Ma, T. Y.; Zheng, Y.; Dai, S.; Jaroniec, M.; Qiao, S. Z. Mesoporous MnCo<sub>2</sub>O<sub>4</sub> with abundant oxygen vacancy defects as high-performance oxygen reduction catalysts. *J. Mater. Chem. A* **2014**, *2* (23), 8676–8682.
- (49) Holze, R. Book Review: *Electrochemical Methods; Fundamentals and Applications*. By Allen J. Bard and Larry R. Faulkner. Wiley Online Library, 2002.
- (50) Antoine, O.; Durand, R. RRDE study of oxygen reduction on Pt nanoparticles inside Nafion®: H<sub>2</sub>O<sub>2</sub> production in PEMFC cathode conditions. *J. Appl. Electrochem.* **2000**, *30* (7), 839–844.
- (51) Chatenet, M.; Génies-Bultel, L.; Aurousseau, M.; Durand, R.; Andolfatto, F. Oxygen reduction on silver catalysts in solutions containing various concentrations of sodium hydroxide-comparison with platinum. *J. Appl. Electrochem.* **2002**, *32* (10), 1131–1140.
- (52) Lin, L.; Zhu, Q.; Xu, A.-W. Noble-metal-free Fe-N/C catalyst for highly efficient oxygen reduction reaction under both alkaline and acidic conditions. *J. Am. Chem. Soc.* **2014**, *136* (31), 11027–11033.
- (53) Zamani, P.; Higgins, D.; Hassan, F.; Jiang, G.; Wu, J.; Abureden, S.; Chen, Z. Electrospun iron-polyaniline-polyacrylonitrile derived nanofibers as non-precious oxygen reduction reaction catalysts for PEM fuel cells. *Electrochim. Acta* **2014**, *139*, 111–116.
- (54) Cao, S.; Han, N.; Han, J.; Hu, Y.; Fan, L.; Zhou, C.; Guo, R. Mesoporous hybrid shells of carbonized polyaniline/Mn<sub>2</sub>O<sub>3</sub> as non-precious efficient oxygen reduction reaction catalyst. *ACS Appl. Mater. Interfaces* **2016**, *8* (9), 6040–6050.
- (55) Chen, R.; Yan, J.; Liu, Y.; Li, J. Three-dimensional nitrogen-doped graphene/MnO nanoparticle hybrids as a high-performance catalyst for oxygen reduction reaction. *J. Phys. Chem. C* **2015**, *119* (15), 8032–8037.
- (56) Huang, D.; Zhang, B.; Li, S.; Wang, M.; Shen, Y. Mn<sub>3</sub>O<sub>4</sub>/carbon nanotube nanocomposites as electrocatalysts for the oxygen reduction reaction in alkaline solution. *ChemElectroChem* **2014**, *1* (9), 1531–1536.

(57) Gaolatlhe, L.; Barik, R.; Ray, S. C.; Ozoemena, K. I. Voltammetric responses of porous  $\text{Co}_3\text{O}_4$  spinels supported on MOF-derived carbons: Effects of porous volume on dopamine diffusion processes. *J. Electroanal. Chem.* **2020**, *872*, 113863.

(58) Zong, L.; Wu, W.; Liu, S.; Yin, H.; Chen, Y.; Liu, C.; Fan, K.; Zhao, X.; Chen, X.; Wang, F.; et al. Metal-free, active nitrogen-enriched, efficient bifunctional oxygen electrocatalyst for ultrastable zinc-air batteries. *Energy Storage Mater.* **2020**, *27*, 514–521.

(59) Ozoemena, K. I.; Mathebula, N. S.; Pillay, J.; Toschi, G.; Verschoor, J. A. Electron transfer dynamics across self-assembled N-(2-mercaptoethyl) octadecanamide/mycolic acid layers: impedimetric insights into the structural integrity and interaction with anti-mycolic acid antibodies. *Phys. Chem. Chem. Phys.* **2010**, *12* (2), 345–357.  
From NLM Medline